Pump and probe waves in dynamic acousto-elasticity: Comprehensive description and comparison with nonlinear elastic theories

J. Rivière,[1,a)] G. Renaud,[2] R. A. Guyer,[1,b)] and P. A. Johnson[1]
[1]*Earth and Environmental Sciences, Los Alamos National Laboratory, Los Alamos, New Mexico 87545, USA*
[2]*Department of Biomechanical Engineering, ThoraxCenter, Erasmus Medical Center, Rotterdam 3000 CA, The Netherlands*

(Received 4 March 2013; accepted 5 July 2013; published online 6 August 2013; publisher error corrected 8 August 2013)

Standard nonlinear ultrasonic methods such as wave frequency mixing or resonance based measurements allow one to extract average, bulk variations of modulus and attenuation versus strain level. In contrast, dynamic acousto-elasticity (DAE) provides the elastic behavior over the entire dynamic cycle including hysteresis and memory effects, detailing the full nonlinear behavior under tension and compression. In this work, we address experimental difficulties and apply new processing methods, illustrating them with a Berea sandstone sample. A projection procedure is used to analyze the complex nonlinear signatures and extract the harmonic content. Amplitude dependences of the harmonic content are compared with existing models. We show that a combination of classical and hysteretic nonlinear models capture most of the observed phenomena. Some differences between existing models and experimental data are highlighted, however. A progressive decrease of the power-law amplitude dependence is found for harmonics larger than the second and for strains larger than 10^{-6}. This observation is related to the phenomenon of acoustic conditioning that brings the material to a metastable state for each new excitation amplitude. Analysis of the steady-state regime provides additional information regarding acoustic conditioning, i.e., a progressive decrease of the amplitude of odd harmonics during excitation time with a log(t)-dependence. This observation confirms that the harmonic content is affected by the conditioning. Experimental challenges addressed include the fact that the compressional mode used for DAE can be affected by bending/torsion modes: their influence is evaluated, and guidances are given to minimize effects. [http://dx.doi.org/10.1063/1.4816395]

I. INTRODUCTION

Probing elastic nonlinearity of materials has broad application including medical imaging, civil engineering, and geophysics, since elastic nonlinearity is a sensitive measure of mechanical damage in solids at many scales. In comparison, standard nonlinear ultrasonic methods such as frequency mixing or resonance based measurements provide the means to extract average variations of modulus and attenuation versus strain level.

In standard (i.e., static) acousto-elasticity, ultrasonic or acoustic waves propagate through the specimen, while it is statically stressed at different amplitudes (uniaxial or hydrostatic stress).[1] For isotropic materials, the speed of sound change with stress levels allows one to extract nonlinear parameters A, B, C, the third order elastic constants.[2] The applied stress is usually only compressive for practical reasons, and static strain levels have to be relatively high to be measured properly ($>10^{-4}$).

Dynamic acousto-elasticity (DAE) employs a low frequency wave source instead of a static device to stress the rod shaped sample at its fundamental compressional mode. Strain levels are therefore smaller ($10^{-8} - 10^{-5}$), and the sample is tested under both compression and tension allowing one to obtain the elastic response over a complete dynamic stress cycle. Previous DAE results[3–5] have shown very complex elastically nonlinear signatures, in particular, hysteretic behaviors and strong effects of material "conditioning."[6,7]

DAE falls under the broad category of "pump-probe" methods that have existed in nonlinear acoustics from at least the 1950s.[8–11] It involves application of two dynamic fields, one to perturb the material elasticity (the "pump") and one to measure the induced elastic changes (the "probe"). DAE uses a low frequency pump (LF field), and the probe is high frequency pulse (HF field).

Our intent in this article is to explore and characterize DAE experimental issues as well as develop new methods for characterizing the probe signal output. First, we compare DAE experimental results with existing models, using a projection procedure to analyze both LF and HF waves. In comparison with previous studies,[3–5] this method is particularly valuable for the HF field because it does not require cumbersome signal processing (filtering, interpolation) to extract information. We therefore minimize the influence of signal processing on results. Differences between experimental data and existing models are highlighted, and the consistency of both fields is evaluated to check the measurement reliability. This procedure can be extended to any arbitrary pump-probe configuration. Second, DAE uses the assumption of a steady-state for the LF field. We assess the LF steady-state

[a)]Electronic mail: riviere_jacques@yahoo.fr
[b)]Also at Department of Physics, University of Nevada, Reno, Nevada 89557, USA.

regime in this study and show that it takes much longer to reach than may be obvious. DAE also makes the assumption of a pure compressional mode for the LF field. Influence of potential adjacent bending/torsional modes is evaluated, and some recommendations are given to minimize such effects. Finally, we evaluate the influence of the LF harmonic content on DAE results.

The experimental method and the projection procedure used to analyze experimental data are presented in Sec. II. A theoretical description of the system is provided in the appendix. The projection procedure is applied in Sec. III A to analyze the harmonic content of both low frequency and high frequency fields and as well as the amplitude dependence. The resonant low frequency field is then analyzed in detail in Sec. III B. The same projection procedure used in Sec. III A allows one to analyze the steady-state regime of the harmonic content. Further, the modal shape of the compressional mode is analyzed, and the influence of potential adjacent torsion/bending modes is discussed.

II. MATERIALS AND METHODS

A. Experimental system

1. DAE setup

The sample shown in Fig. 1(a) and used to illustrate the developments described here is a cylinder of room-dry Berea sandstone, length $L = 15\,\text{cm}$ and diameter $d = 2.54\,\text{cm}$, that stands upright on a low frequency compressional source, a piezoceramic disk. Berea is a very well known and well characterized material in geophysical studies (e.g., (Ref. 6)). A high frequency compressional source and associated receiver straddle the sample at height $h = 2\,\text{cm}$ above the base. A light accelerometer, placed on the top of the sample (free surface), monitors the low frequency wave field. The essential idea is to have a high frequency broadcast, from ultrasonic source to ultrasonic receiver, to probe the elastic state that is modulated in the sample by the low frequency source.

The low frequency source has diameter greater than d and creates a strain field $\epsilon_x(x,t)$ in the sample that is primarily a function of x, the vertical dimension. Typically, the low frequency f_{LF} is the frequency of the lowest compressional resonant mode of the cylinder, $f_{LF} = c/(4L)$ with fixed-free boundary conditions (wavelength $\lambda = 4L$), and where c is the nominal compressional sound speed in the sample (roughly 2400 m/s, that is $f_{LF} \simeq 4000\,\text{Hz}$). The strain field is sampled at $x = h$ by the high frequency broadcast that crosses the sample in time, t_{US}, of order $d/c \simeq 10\,\mu\text{s}$. During the high frequency wave travel time the low frequency strain field changes very little, $t_{US}/T_{LF} = d/(4L) = 2.54/60 \simeq 0.04$, with $T_{LF} = 1/f_{LF}$. This first condition is required to assume an acousto-elastic effect ($t_{US} \ll T_{LF}$). Further, the width of US beam is approximately the diameter of the US transducer ($d_{US} = 6\,\text{mm}$). Thus, we can assume that the strain established in the sample by the low frequency source is constant spatially over the US beam width ($d_{US}/\lambda = 0.6/60 = 0.01$).

Assuming fixed-free boundary conditions, the strain is maximum at $x = 0$ and can be evaluated from the acceleration measured at the top of the sample using $\epsilon_x(0,t) = -\ddot{u}_x(L,t)/(8\pi L f_{LF}^2)$. In the following, we will assume that the strain at $x = h$ is roughly equal to the strain at the base, i.e., $\epsilon_x(h,t) \simeq \epsilon_x(0,t)$. Further, this formula is only valid if most of the acceleration content is at the fundamental frequency f_{LF}. These choices will be discussed later in Sec. III B 2. Finally, it is important to note that ultrasound pulses are launched in the sample near the fixed boundary because the maximum strain amplitude is expected at this location.

The high frequency source at 1 MHz is a pulse of duration $3\,\mu\text{s}$, i.e., three high frequency periods. The low frequency broadcast/detection and the high frequency

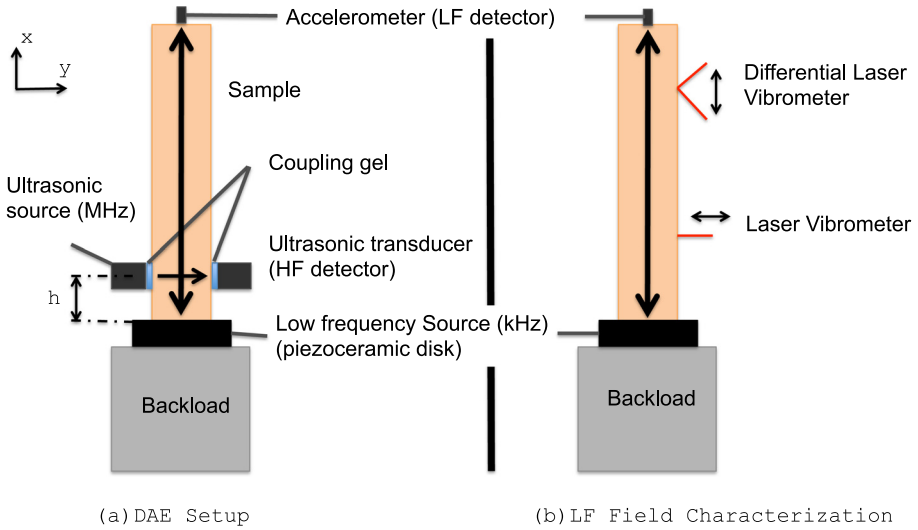

FIG. 1. Experimental setup. (a) DAE setup. The low frequency source resonates the sample on its first compressional mode (≃4000 Hz), with fixed-free boundary conditions. Ultrasound pulses at 1 MHz are launched in the sample simultaneously to probe the sample at a given strain level imposed by the low frequency field. An accelerometer placed on the top of the sample allows to measure the low frequency field, whereas a second ultrasonic transducer detects the high frequency pulses. (b) LF field characterization setup (results in Sec. III B 2). Either a differential laser vibrometer or a standard laser vibrometer are used to measure axial (x-direction) or radial (y-direction) particle velocities, respectively, along the sample length, while the sample resonates on its first compressional mode.

broadcast/detection are controlled by a central clock. Both detections are sampled at 50 MHz.

2. LF field characterization setup

As described in Fig. 1(b), a laser vibrometer can also be deployed to measure the vector velocity field of the sample sides during activation of the LF source at the frequency of the first compressional mode. Either a differential laser vibrometer or a standard laser vibrometer are used to measure axial (x-direction) or radial (y-direction) particle velocities, respectively, along the sample length. The spatial structure of the LF field and the influence of potential adjacent torsion/bending modes can be then evaluated from this measurement. Also, the spatial structure of harmonics within the bar can be compared with theoretical predictions (see Sec. III B 2).

B. Measurement protocol

The DAE measurement protocol involves the following ingredients. At time $t = t_0 = 0$, the high frequency source is turned on, sending a sequence of 1 MHz pulses at times t_j. The time between successive pulses, ΔT, is chosen such that the coda signal received in response to the j^{th} pulse decays to zero before sending the $(j+1)^{th}$ pulse, $\Delta T \simeq 0.1$ ms. From the complete ultrasonic signal received by the high frequency detector, one extracts the direct wave, i.e., the 3 first periods of each received pulse $s(t - t_j)$.

The low frequency source with amplitude A is only turned on after 5 ms, allowing several ultrasonic pulses to propagate within the sample without being disturbed by the low frequency field. The signal at the sample top is recorded at times t_i. The signal measured at t_i, an acceleration, is related to the displacement field at the sample top and to the nominal strain field $\epsilon_x(t_i)$ in the sample, as described earlier.

For Berea sandstone, the steady-state is reached after roughly 100 ms of LF vibration (Fig. 2(a)). Each pulse $s(t - t_j)$ propagating during the steady-state can be compared with the pulses that cross the sample before activation of the low frequency source. The spacing ΔT is chosen to be incommensurate with T_{LF} so that over time the broadcasts at the set of times $\{t_j\}$ sample all phases of the $\epsilon_x(t_i)$ strain field.

The first step in analysis of the $s(t - t_j)$ is to compare the first reference pulse $s(t - t_0)$ by employing cross-correlation

$$C(\tau_j, t_j) = \int_0^\infty s(t - t_0)s(t + \tau - t_j)dt \tag{1}$$

to determine $\tau(t_j)$, the shift in the time of flight of the high frequency pulse as it crosses the sample at time t_j.[12,13] The shift $\tau(t_j)$ is refined by interpolating the peak of the cross-correlation function with a second order polynomial function to obtain subsample time resolution.[14] Three points are considered for this interpolation: the maximum of the cross correlation function and the two adjacent points. Assuming that dynamic variations in the sample diameter (i.e., the probe path) due to Poisson effect are negligible,[15] time of flight modulations can be converted into a relative velocity change using

$$\frac{\Delta c}{c}(t_j) = -\frac{\tau(t_j)}{t_{US}^0}, \tag{2}$$

where t_{US}^0 is the time of flight of the reference pulse. Finally, the change in the relative sound speed is associated with the strain field at $x = h$ at the moment of the high frequency

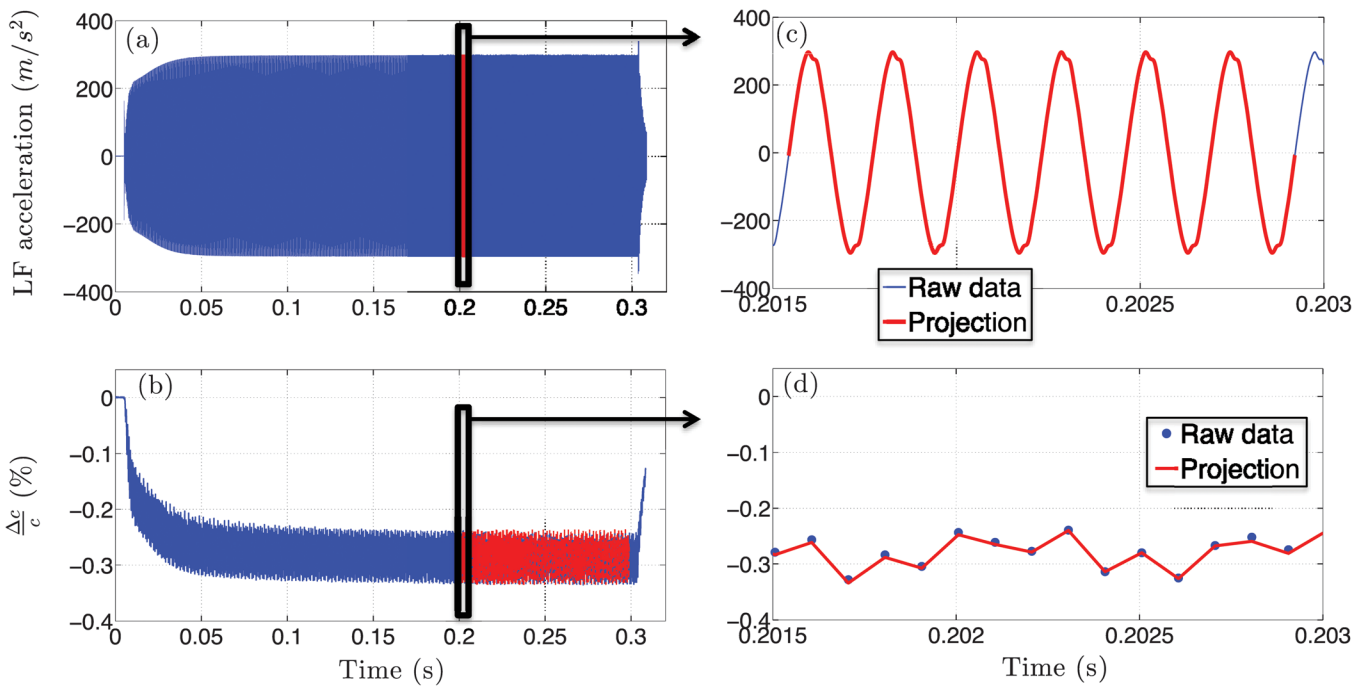

FIG. 2. Examples of projection procedure. Low frequency acceleration (a) and high frequency velocity change (b) as a function of time for Berea sandstone in solid blue line. Red curves are the result of the projection procedure [using $N = 15$ in (a) and $N = 14$ in (b)]. Acceleration of 300 m/s^2 corresponds roughly to a 4×10^{-6}-strain (see formula Sec. II A). (c) and (d) are zooms in time of (a) and (b), respectively. The low frequency acceleration is sampled at 50MHz, and thus, the projection procedure can therefore be applied to a small number of periods of the signal as necessary [for example, 6 periods as seen in (c)]. On the other hand, the velocity change signal is a down sampled signal at the pulse frequency rate (10 kHz here). A much longer signal is therefore needed to apply the projection procedure successfully [from 200 to 300 ms here as seen in (b)].

broadcast, i.e., $\frac{\Delta c}{c}(t_j) \Longleftrightarrow \epsilon_x(h,t_j)$ where the latter term $\epsilon_x(h,t_j)$ is a down-sampled version of $\epsilon_x(h,t_i)$.

Each DAE signature presented in Sec. III is the average of ten acquisitions, and we wait 30 s between each pump excitation. This waiting time is chosen long enough to ensure that most of the relaxation has taken place (slow dynamics[7]) but short enough to perform measurements in stable environmental conditions (the slow dynamics may continue for minutes or hours after the sample is perturbed; however, most for the relaxation takes place very rapidly, within the first 10-20 s).

C. Signal analysis: Projection procedure

The dynamic acousto-elastic experiment allows one to obtain two temporal signals, i.e., the low frequency acceleration $\ddot{u}_x(t_i)$, and the relative change in ultrasonic speed of sound $\frac{\Delta c}{c}(t_j)$. The harmonic content of the former could be analyzed with a standard Fourier transform, whereas the latter one is a down sampled signal (at the frequency of the US pulse repetition rate, *cf* Fig. 2(d)) that has to be analyzed with a different method. The method used here called the projection procedure will be applied to both high and low frequency signals for convenience. It consists in projecting the signals onto a series of orthonormal functions at given frequencies

$$\begin{aligned} S_n(t_k) &= q_n \sin(n\omega t_k) \\ C_n(t_k) &= r_n \cos(n\omega t_k) \quad \text{with} \quad n = 1,2,...,N, \end{aligned} \tag{3}$$

where ω is the low frequency pulsation at which the sample is driven and N being chosen depending on the harmonic content of the signal. Time t_k can denote t_i or t_j, depending on the studied function. The low frequency acceleration is sampled at 50 MHz ($t_{i+1} - t_i = 20$ ns), and thus, the projection procedure can be applied to a small number of periods of the signal as necessary. On the other hand, the velocity change signal is a down sampled signal at the pulse frequency rate (10 kHz here, $t_{j+1} - t_j = \Delta T \simeq 0.1$ ms). A much longer signal is therefore needed to apply the projection procedure successfully. Amplitudes q_n and r_n have to be chosen such that these functions are orthonormal

$$\begin{aligned} \langle S_m | S_p \rangle &= \delta_{m,p} \\ \langle C_m | C_p \rangle &= \delta_{m,p} \\ \langle S_m | C_p \rangle &= 0, \end{aligned} \tag{4}$$

where $\delta_{m,p}$ is the Kronecker symbol ($\delta_{m,p} = 1$ if $m = p$, 0 otherwise) and $\langle | \rangle$ denotes the scalar product. Practically, q_n and r_n are found using the numerical Gram-Schmidt process (see appendix C).

If the studied signal is denoted $f(t_k)$ and the result of the projection is denoted $f_p(t_k)$, then $f_p(t_k)$ is given by

$$f_p(t_k) = \sum_{n=1}^{N} a_n S_n(t_k) + \sum_{n=1}^{N} b_n C_n(t_k), \tag{5}$$

where coefficients a_n and b_n are

$$\begin{aligned} a_n &= \langle S_n | f \rangle \\ b_n &= \langle C_n | f \rangle. \end{aligned} \tag{6}$$

Coefficients a_n and b_n tell how much of the n^{th} harmonic is present in the signal. Assuming that the response at the fundamental frequency is a sine function, the quantity $A_1 = a_1 q_1$ tells us how much of the signal remains in phase with the fundamental, whereas the amplitude $B_1 = b_1 r_1$ tells us how much is in quadrature. Practically, the magnitude $R_n = \sqrt{A_n^2 + B_n^2}$ can be used to quantify the harmonic content. In the following, quantity R_n will be denoted $u_{n\omega}$ for the low frequency signal (acceleration is converted into displacement after projection) and $\frac{\Delta c}{c}|_{n\omega}$ for the high frequency signal. Both quantities will be plotted as a function of $u_{1\omega}$ which corresponds to the amplitude displacement of the driving fundamental frequency.

In case of a purely linear system, the LF signal should only contains the fundamental u_ω, whereas the high frequency signal $\frac{\Delta c}{c}$ should be 0 (no change in the speed of sound across the sample). Further, in the case of a purely quadratic elastic nonlinearity (appendix A 1), the low frequency signal should contain u_ω and $u_{2\omega}$ (fundamental and second harmonic, respectively), while the HF signal should only contain $\frac{\Delta c}{c}|_\omega$.

III. EXPERIMENTAL RESULTS

A. Consistency of LF and HF wave fields, parameter scaling observations, and comparison with existing models

1. Harmonic content

a. Decomposition. An example of projection result is displayed in Fig. 2 for both low and high frequency fields as a function of time, for a dry Berea sandstone sample. LF acceleration and HF velocity change are displayed as a function of time in Figs. 2(a) and 2(b), respectively. Red curves are the result of the projection procedure. Figs. 2(c) and 2(d) are zooms in time of Figs. 2(a) and 2(b), respectively. The low frequency acceleration is sampled at 50MHz, and thus, the projection procedure can therefore be applied to a small number of periods of the signal as necessary (for example, 6 periods as seen in Fig. 2(c)). On the other hand, the velocity change signal is a down sampled signal at the pulse frequency rate (10 kHz here). A much longer signal is therefore needed to apply the projection procedure successfully (from 200 to 300 ms here as seen in Fig. 2(b)). Results presented in this section correspond to projections that are applied over the complete steady-state, i.e., between 0.1 and 0.3 s in Fig. 2.

The projection is first applied for different values of N at one high strain amplitude (8×10^{-6}), where the response is highly elastically nonlinear. This allows one to decide how many functions are needed to track the harmonic content. The root mean square error that quantitatively evaluates the difference between experimental data and the projection result is displayed in Fig. 3 for LF and HF fields as a function of N. For the LF field in Fig. 3(a), the error remains constant and small for $N \geq 15$. For the HF field, the error reaches

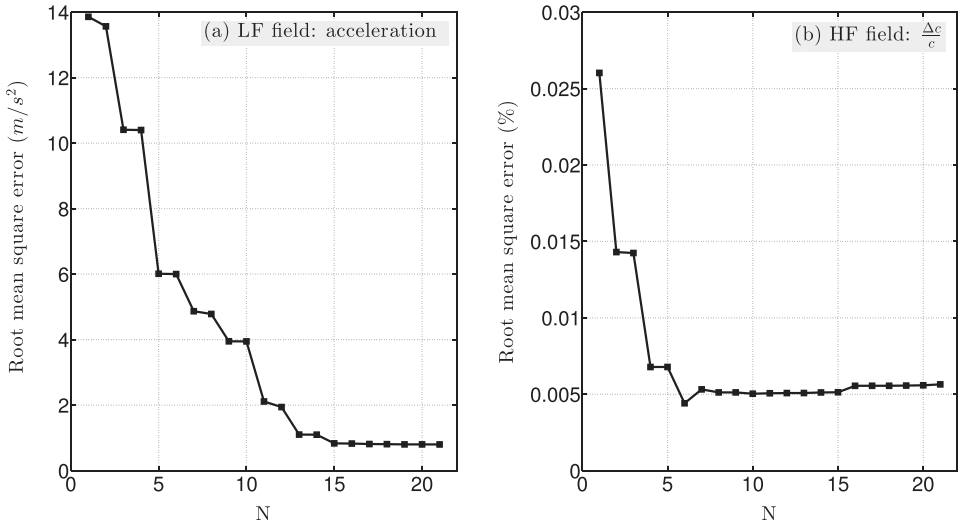

FIG. 3. Projection quality. The root mean square error quantitatively evaluates the difference found between the projection result and experimental data at high strain amplitude (8×10^{-6}), when the response is highly nonlinear. (a) Root mean square error found for the LF acceleration as a function of N (Eq. (3)). The error remains constant and small for $N \geq 15$. We also observe a step-like behavior, because odd harmonics dominate over even ones. (b) Same curve for the HF relative velocity change. The curve reaches a minimum for $N = 6$.

a minimum for $N = 6$ and slightly increases for higher N. A plateau is found for $8 \leq N \leq 15$. The error then increases for $N > 15$. This increase is due to the fact that the signal is not long enough in time to track the highest harmonics. For both curves, we observe a step-like behavior, because odd harmonics dominate over even ones. Based on this result, we decide to use $N = 15$ and $N = 14$ for LF and HF fields to track the signal content until the 15*th* harmonic. We observe good agreement in Fig. 2 between experimental data and projection results. Projection results of $\frac{\Delta c}{c}$ for 26 increasing low frequency excitation amplitudes ranging from 3×10^{-8} to 8×10^{-6} in strain are shown in Fig. 4. We also check that the projection result fits experimental data.

Amplitudes $\frac{\Delta c}{c}|_{n\omega}$ and $u_{n\omega}$ extracted from the projection procedure allow us in a first approach to compare the harmonics in both the LF and HF fields without taking into account the complex signatures of Fig. 4, in particular, hysteretic behaviors.

b. Second harmonic. In Fig. 5, the amplitudes $\frac{\Delta c}{c}|_{\omega}$ and $u_{2\omega}$ are shown as a function of the fundamental driving displacement $u_{1\omega}$ on a log-log scale. We note that $\frac{\Delta c}{c}|_{\omega} \propto u_{\omega}$ for the entire displacement amplitude range and $u_{2\omega} \propto u_{\omega}^2$ for displacement amplitudes higher than the noise level (between 10^{-13} and 10^{-12} at 2ω for the lowest amplitudes of excitation). These two scalings are predicted by the quadratic nonlinear elastic model described in appendix A 1, assuming an isotropic sample.

Components in phase and 90° out of phase with the fundamental displacement are also displayed in Fig. 5. We note that the LF 2ω-signal measured at the free end of the bar is 90° out of phase with the fundamental, when it exceeds the noise level (Fig. 5(b)). This result is also predicted by the quadratic nonlinear elastic model (appendix A 2).

c. Third and higher harmonics. Fig. 6 shows the same projection results as Fig. 5 up to the seventh harmonic (only

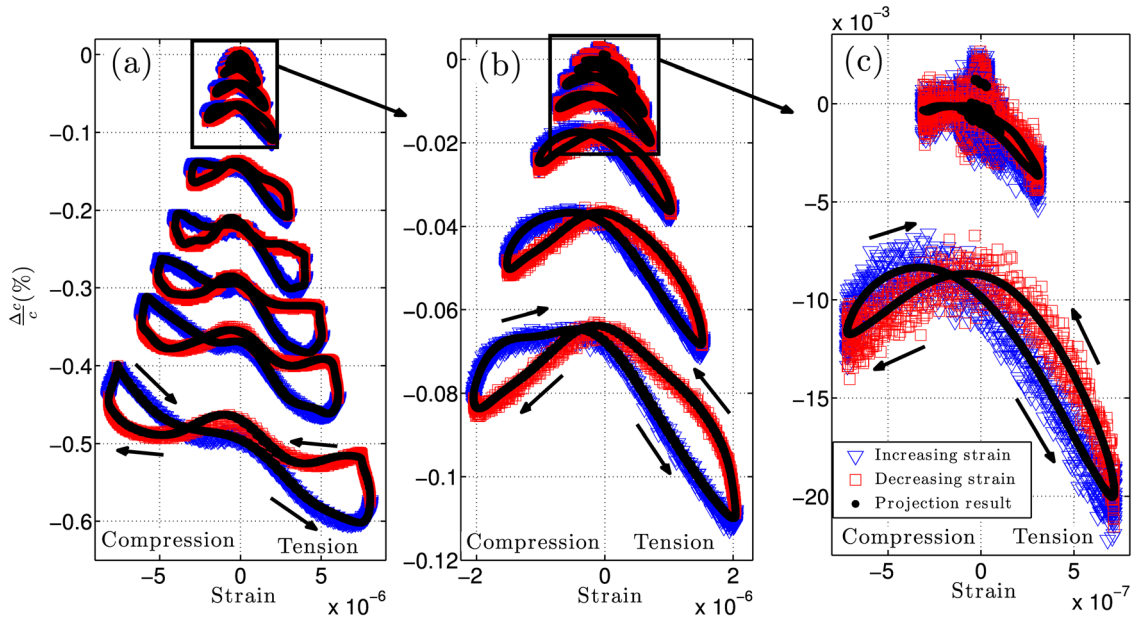

FIG. 4. High frequency velocity change $\frac{\Delta c}{c}$ as a function of low frequency strain ϵ_x in Berea sandstone for 26 increasing low frequency excitations ranging from 3×10^{-8} to 8×10^{-6} in strain. Some amplitudes are removed at several strain levels for clarity. Progressive zooms of the low amplitude signals are shown in (b) and (c), respectively. Blue triangles and red squares correspond to increasing and decreasing strains, respectively. The black line shows the result of the projection procedure for each curve.

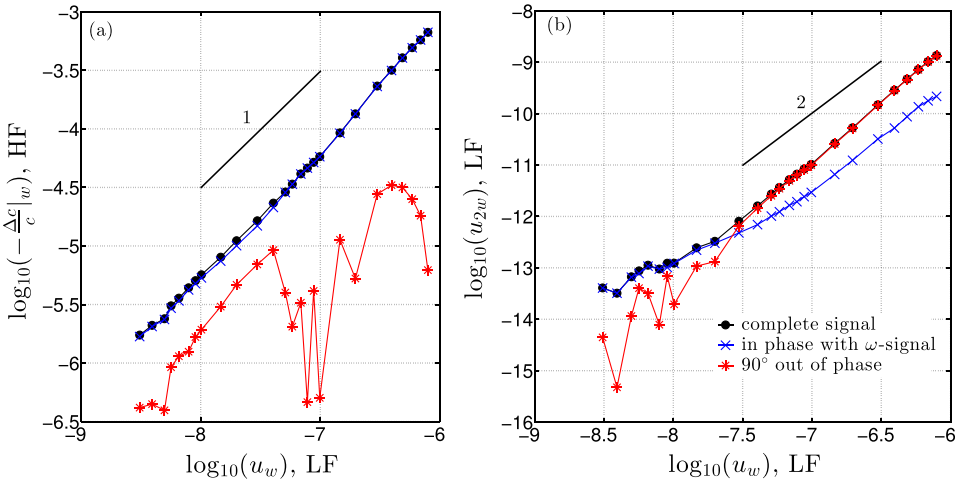

FIG. 5. Amplitude dependences obtained in Berea sandstone for both HF (relative velocity change in (a)) and LF (displacement u in (b)) fields that can be compared with quadratic nonlinearity described in appendix A 1. The complete signal (black), the in phase (blue), and 90° out of phase (red) components are shown. Respective scalings of 1 and 2 correctly fit the quadratic nonlinear model. The 90° out of phase portion is dominant for the LF field, as found theoretically in appendix A 2.

7 harmonics out of 15 are displayed for figure clarity). Amplitude dependences are complex for harmonics higher than the second one. We note that $\frac{\Delta c}{c}|_{2\omega} \propto u_\omega^2$ for displacements below 100 nm (strain $< 10^{-6}$), while $u_{3\omega} \propto u_\omega^2$ for the LF field. A second primary observation is the dominance of odd harmonics over even ones, i.e., $u_{3\omega} > u_{5\omega} > u_{7\omega} > u_{4\omega} > u_{6\omega}$ for the LF field. The same observation is made for the HF field, which confirms the consistency between LF and HF fields. Highest harmonics ($n > 3$) emerge from noise level for displacements higher than 50 nm, i.e., roughly 5×10^{-7} in strain for both fields.

The classical nonlinear theory extended to fourth-order elastic constants predicts the square dependence of $\frac{\Delta c}{c}|_{2\omega}$. This same theory would predict a cubic dependence for $u_{3\omega}$, while the dependence found is quadratic. This latter scaling is predicted by hysteretic models[16] (appendix B).

In Figs. 7(a)–7(c), amplitude dependences of odd harmonics for the LF field are displayed (same as Fig. 6(b)). A quadratic dependence with fundamental amplitude is approximately found for $u_{3\omega}$ and $u_{7\omega}$. A higher order power-law dependence—between 4 and 5—is found for $u_{5\omega}$. In phase and 90° out of phase components with the fundamental are also displayed. The 90° out of phase component dominates for $u_{7\omega}$ whereas in phase component is dominating for $u_{5\omega}$. No clear trend can be determined for $u_{3\omega}$ since each component alternatively dominates from one excitation amplitude to another.

Dependences of odd harmonics can be compared with quadratic hysteretic nonlinearity described in appendix B. A quadratic dependence of all odd harmonics with fundamental amplitude is expected with this model, as found for third and seventh harmonics. Further, odd harmonics are expected to be 90° out of phase with the fundamental according to this theoretical description. This is only the case for the seventh harmonic. In Fig. 7(d), the LF waveform experimentally obtained for the highest strain amplitude is compared with the triangular waveform expected with hysteretic nonlinearity[16] and with a linear sine function. We observe a "localized" nonlinear distortion when maximum strain is reached, as opposed to the theoretical predicted triangular waveform. This

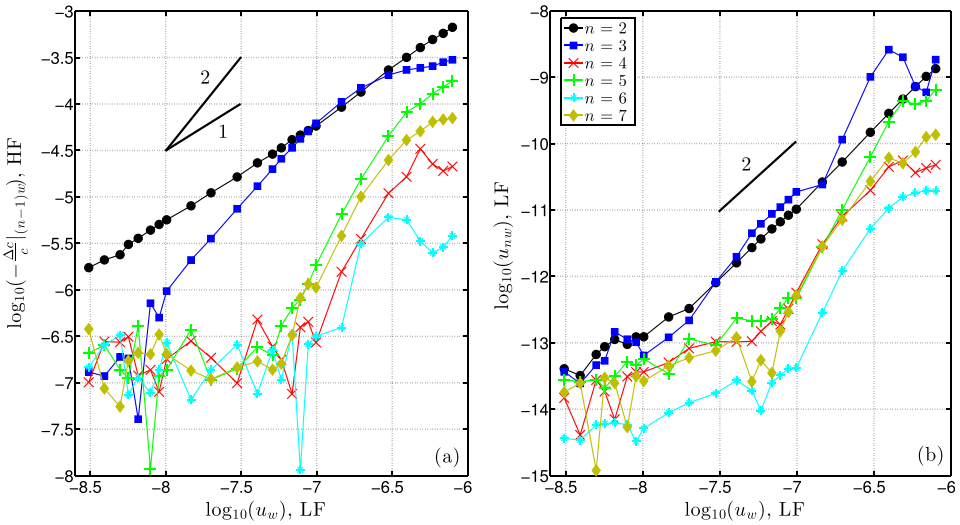

FIG. 6. Same as Fig. 5 for the first seven harmonics. Amplitude dependences obtained in Berea for both high frequency (relative velocity change in (a)) and low frequency (displacement u in (b)) fields. Analysis of amplitude dependences is complex for harmonics higher than for the second one. Most of higher harmonics emerge for displacements higher than 50 nm, i.e., roughly 5×10^{-7} in strain. If the second harmonic fits correctly the nonlinear quadratic model, higher harmonics are more in accordance with hysterectic models since odd harmonics have much higher amplitudes than even ones. Also, scaling of the second harmonic is constant over the entire displacement range, whereas scalings of higher harmonics tend to decrease for the highest amplitudes. This last feature is particularly visible for the HF field (a).

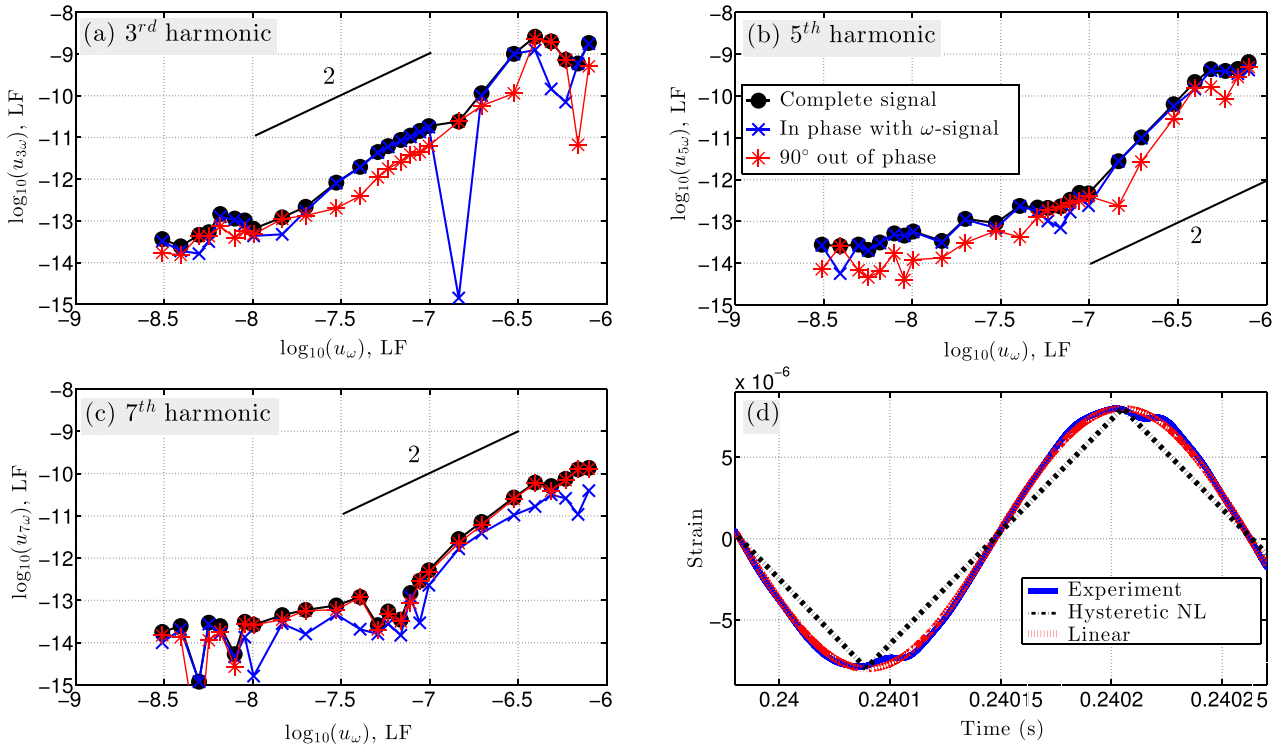

FIG. 7. Odd harmonics, LF field. (a)-(c) Amplitude dependences obtained in Berea sandstone for odd harmonics (third, fifth, and seventh, respectively) of LF field that can be compared with hysteretic nonlinearity described in appendix B. Expected quadratic dependence with fundamental amplitude is approximately found for the third and seventh harmonics. Higher order dependence is found for the fifth. In phase and out of phase components with the fundamental are also displayed. Odd harmonics are expected to be 90° out of phase with the fundamental for hysteretic nonlinearity. It is only the case for the seventh harmonic. (d) The LF waveform experimentally obtained for the highest strain amplitude is compared with a linear sine function and the triangular shape of hysteretic nonlinearity.[16] We observe a very localized in time nonlinearity (e.g., the dip in strain at $t \simeq 0.2401$ s and $t \simeq 0.24022$ s) when strain reaches an extremum, as opposed to the theoretical triangular waveform. This difference explains why harmonics are not found 90° out of phase with the fundamental. At zero strain ($t \simeq 0.24015$ s), the experimental and sine functions match well, meaning that the nonlinear contribution is almost only present at extreme strains.

difference explains why harmonics are not systematically found 90° out of phase with the fundamental. Further at zero strain ($t \simeq 0.24015$ s) in Fig. 7(d), the experimental and sine functions match well, bearing out that the nonlinear contribution is mainly present at extreme strains.

d. Modeling of the harmonic content. To describe these results with existing models, one can use the following 1D-Eq. [16]

$$M = M_0(1 + \beta\epsilon + \delta\epsilon^2 + ... + \alpha(\epsilon_m + sign(\dot{\epsilon})\epsilon)), \quad (7)$$

where M, M_0, ϵ, β, δ are, respectively, the generic nonlinear modulus, the linear modulus independent of the strain wave amplitude, the strain amplitude, the nonlinear quadratic term and the nonlinear cubic parameter. β and δ are from the classical nonlinear theory (appendix A). The last term of the equation is related to the quadratic hysteretic nonlinear theory (appendix B) and involves α, $\dot{\epsilon}$, and ϵ_m: the nonlinear hysteretic parameter, the strain rate and the maximum strain excursion experienced by the material, respectively. The maximum strain excursion in our case is the amplitude of the low frequency resonance. Experimental results suggest that the quadratic nonlinear theory can explain the amplitude dependence of the second harmonic ($n = 2$). On the other hand, dominance of odd harmonics for strain higher than 5×10^{-7} suggests the hysteretic model involving only odd harmonics is more appropriate. A combination of both classical and hysteretic models with specific strain thresholds could be then a first appropriate start to model the experiment.[17] The behavior observed for the amplitude dependence of the third harmonic also confirms this combination. Indeed, the third harmonic ($n = 3$) of the high frequency field seems to be predicted by the classical theory for strain roughly below 10^{-6} (scaling of 2 in Fig. 6(a)), whereas the low frequency field could be predicted by the hysteretic model in Fig. 6(b) (scaling of 2). This transition from classical to hysteretic behavior is coherent with previous studies, e.g., (Refs. 3 and 18).

It is worth noting here that the LF field probes the entire sample (including the bonding of the sample on the LF source), whereas the high frequency observation results from the interaction between the pump and the probe, therefore, probing the sample locally. The consistency of both fields is made under the assumption of a homogenous material, a linear LF source and a bonding that does not produce significant nonlinear effects. In particular, we have observed more inconsistency for the LF field when bonding/debonding the sample: in that sense HF field observations are therefore more reliable.

One last observation concerns the highest amplitude excitations. We observe in Fig. 6 that the scaling found for the second harmonic is constant over the entire displacement range, whereas scalings of higher harmonics tend to decrease as the driving amplitude increases. This is particularly visible for the high frequency field in Fig. 6(a). In particular, the curvature in the diagram $\frac{\Delta c}{c}$ *vs* strain (Fig. 4) related to the third harmonic

(term δ) clearly decreases for increasing excitation amplitudes. This observation has already been reported experimentally in Lavoux Limestone for the third harmonic of the HF signal (cubic nonlinearity), but has not been observed for higher harmonics previously.[3] It was also observed numerically that the wave propagation into a nonlinear hysteretic medium leads to a "saturation" of the third harmonic (Fig. 15 of Ref. 16). It is remarkable that for both fields the second harmonic is not affected by this change in amplitude dependence. As far as the third harmonic is concerned, it means that the cubic elastic nonlinear model is not suitable for strain higher than 2 or 3×10^{-6} in Berea sandstone (in agreement with.[18]) For the HF field which corresponds to the probe signal (Fig. 6(a)), we believe that the change in amplitude dependence is due to the acoustic conditioning, as previously suggested in Refs. 3 and 18. This reversible acoustically induced conditioning brings the material to a new metastable state for each new excitation amplitude, which affects the scalings for all the harmonic content with the exception of the second one (see also discussion related to Figs. 9 and 11). Amplitude dependent attenuation coming from the hysteretic nonlinearity could also be an effect for the harmonic content of the LF resonance (Fig. 6(b)), as observed numerically in the configuration of wave propagation.[16] Therefore, both acoustic conditioning and nonlinear attenuation are responsible for scaling changes of the LF field. To date, we do not know which mechanism is dominant.

The theory presented in appendix B is based on a uniform distribution of elementary hysteretic elements. An approach based on Preisach-Mayergoyz description (PM space) using a non uniform distribution could help in describing the harmonic content.[19,22,33] The distribution would consist in less hysterons (elementary hysteretic units) at higher strains to reach a saturation of harmonics (Fig. 12.3 of Ref. 19, Type G distribution). However, we note that this approach would not properly describe the observation made in Secs. III A 2 and III B 1 (Figs. 9 and 11). Table I aims at summarizing the ability of the main different models to describe observations made in DAE. In addition to the harmonic content, observations made in Secs. III A 2 and III B 1 are also present in the table (see discussion in the respective sections).

2. Offset and $\frac{\Delta c}{c}$-intercept

a. Observations. DAE allows one to distinguish two features that standard nonlinear methods (e.g., resonance based measurements) cannot discriminate. In Fig. 4 (also in Fig. 2(b)), we first observe an average decrease in the relative velocity change ("offset"), meaning that $\frac{\Delta c}{c}|_{0\omega}$ decreases when strain amplitude increases. Simultaneously, the relative velocity change is not zero when strain is zero: $\frac{\Delta c}{c}$-intercept (or $\frac{\Delta c}{c}|_{\epsilon=0}$) also decreases with increasing strain amplitude. These two observations are concomitant and their quantity is almost identical. From Eq. (7), if we assume a linear

TABLE I. Ability of different models to describe observations made with DAE experiments. We note that quadratic and cubic elastic nonlinear models, as well as the soft-ratchet model[24] in its current form do not account for nonlinear attenuation observed experimentally.[13,15] We also note that some other models exist, taking into account dispersion phenomenon (not measured in this experiment)[25–28] or those based on contact mechanics.[17,29]

Observations → Models ↓	Slope in diagram $\frac{\Delta c}{c}$ *vs* ϵ[15]	Curvature (Fig. 9(a))	Hysteresis (Fig. 9(b))	Offset $\left(\frac{\Delta c}{c}|_{0\omega}\right)$	$\frac{\Delta c}{c}$-intercept $\left(\frac{\Delta c}{c}|_{\epsilon=0}\right)$	Dominance of odd harmonics (Fig. 6)	Scaling change[a] (Fig. 6)	Decrease in odd harm during steady-state (Fig. 11)
Quadratic[16,20]	**yes**	no	no	no	no	no	no	no
Cubic[16,21]	no	**yes**	no	**yes**, partly (Eq. (8))	no	**yes**	no	no
Uniform PM space[16]	no	no	**yes**	**yes**, but overestimation of the hysteresis (see Fig. 9(b))		**yes**	**yes**[b]	no
Non uniform PM space[22]	**yes**[c]	**yes**[c]	**yes**			**yes**	**yes**	no
Uniform PM space w/elastic and rigid states[23]	no	no	**yes**	**yes**	**yes**	**yes**	**yes**[b]	?
Soft-ratched[24]	no	no	**yes**	**yes**	**yes**	probably, if the model is extended to the harmonic frequencies		?

Note: The "yes" are emphasized in bold type to facilitate the reading of the table.
[a]Nonlinear attenuation due to the cascade of harmonic generation excluded.
[b]Scaling change coming from NL attenuation due to hysteresis.[16]
[c]Non uniform distribution of non hysteretic units located on the diagonal of the PM space can lead to a quadratic and/or cubic elastic nonlinearity.

excitation $\epsilon = \epsilon_m \sin(\omega t)$, the offset is calculated taking the average velocity over one period

$$\left.\frac{\Delta c}{c}\right|_{0\omega} = \left.\frac{1}{2}\frac{\Delta M}{M}\right|_{0\omega} = \frac{\delta \epsilon_m^2}{4} + \frac{\alpha \epsilon_m}{2}, \tag{8}$$

while the $\frac{\Delta c}{c}$-intercept is found replacing ϵ by zero in Eq. (7)

$$\left.\frac{\Delta c}{c}\right|_{\epsilon=0} = \left.\frac{1}{2}\frac{\Delta M}{M}\right|_{\epsilon=0} = \frac{\alpha \epsilon_m}{2}. \tag{9}$$

The only difference between both features is the cubic nonlinearity containing δ, responsible for the curvature in Fig. 4. At low strain excitation when the curvature in Figs. 4(b) and 4(c) is strong (high and constant δ value), the offset is larger than the $\frac{\Delta c}{c}$-intercept, i.e., $\frac{\Delta c}{c}|_{0\omega} > \frac{\Delta c}{c}|_{\epsilon=0}$. For high strain amplitude in Fig. 4(a) when the curvature vanishes, both values are similar, $\frac{\Delta c}{c}|_{0\omega} \simeq \frac{\Delta c}{c}|_{\epsilon=0}$. The change in curvature can be seen as a decrease in δ ($\delta \to 0$), which means that the cubic elastic nonlinear model is not suitable for strain higher that 2 or 3×10^{-6}.

For strain as high as 10^{-5}, the relative velocity change can decrease by 0.5% in Berea sandstone (Fig. 4). As shown in Fig. 8, experimental results in several rocks give a nearly square amplitude dependence for the offset.

b. Comparison with classical nonlinear theory. The quadratic elastic nonlinear model does predict the presence of a non zero $\frac{\Delta c}{c}|_{\epsilon=0}$ or $\frac{\Delta c}{c}|_{0\omega}$ (identical in this case).[30,31] This term is not described by Eqs. (7)–(9), but is concomitant with the creation of the second harmonic ($\beta \neq 0; \omega + \omega \to 2\omega$; $\omega - \omega \to 0\omega$, with $u_{0\omega} \simeq 2u_{2\omega}$), however, values found in rocks are orders of magnitude higher than what the model predicts. For comparison, using $u_{0\omega} \simeq 2u_{2\omega} = 2.6\,\text{nm}$ for the highest amplitude of excitation as found in Fig. 5(b) (i.e., $\beta \simeq 10^2$), the expected relative length change (equivalent to a static strain) is roughly $u_{0\omega}/L = 10^{-6}\%$, five orders of magnitude lower than the observed relative velocity change (0.5%). Furthermore, the physical phenomenon is different since the offset observed in undamaged materials with atomic based nonlinearity is due to a length change,[30,31] whereas typical 0.5%-drops observed in rocks or damaged materials are primarily due to speed of sound change, i.e., a softening of the modulus. Another difference is the fact that the post excitation recovery, often called slow dynamics, is much longer[3,7,32] than relaxation observed in undamaged materials, i.e., the modulus recovers within minutes, hours or days, *vs* microseconds or less for the length recovery.[31]

Second, the classical nonlinear theory extended until the cubic term ($\delta \neq 0$) gives an offset in the HF field having a square-law dependence with fundamental amplitude ($\delta\epsilon^2/4$ in Eq. (8)) and a zero $\frac{\Delta c}{c}|$-intercept. In Fig. 9(a), the experimental curve is the same as the one presented in Fig. 4 for an intermediate amplitude of excitation ($\epsilon = 10^{-6}$). Coefficient $\delta = -2.10^8$ is chosen such that curvatures of the experimental data and the model are similar. The cubic elastic nonlinear model does not predict a non zero $\frac{\Delta c}{c}$-intercept as found in the experiment.

c. Comparison with quadratic hysteretic nonlinear theory (uniform PM space). Finally, the quadratic hysteretic nonlinear model ($\alpha \neq 0$) predicts an average softening of materials equal to the $\frac{\Delta c}{c}$-intercept ($\frac{\Delta c}{c}|_{0\omega} = \frac{\Delta c}{c}|_{\epsilon=0} = \frac{\alpha\epsilon_m}{2}$, as seen in Eqs. (8) and (9)). Fig. 9(b) compares the nonlinear signature obtained at the highest strain amplitude (also visible in Fig. 4(a) with the typical bow-tie obtained for the hysteretic model.[33] As predicted by this model, signatures obtained at high strain amplitudes have an offset roughly equal to the $\frac{\Delta c}{c}$-intercept ($\frac{\Delta c}{c}|_{0\omega} \simeq \frac{\Delta c}{c}|_{\epsilon=0}$). The value $\alpha = -1200$ in Fig. 9(b) is fit such that both experimental and modeling curves have the same average softening modulus, while ϵ_m is set to the maximum strain experienced by the material (8×10^{-6} in Fig. 9). Both curves present a bow-tie signature, however, one clearly observes that if the model is set at the same average velocity, the hysteresis predicted by the model becomes much bigger than what is found in the experiment.

d. Other hysteretic nonlinear theories. The observed experimental $\frac{\Delta c}{c}$-intercept is associated with the phenomenon of conditioning, widely reported earlier with other experimental methods[7,32,34–36] and DAE.[3] Indeed, each larger excitation amplitude takes the material to a metastable state[18]

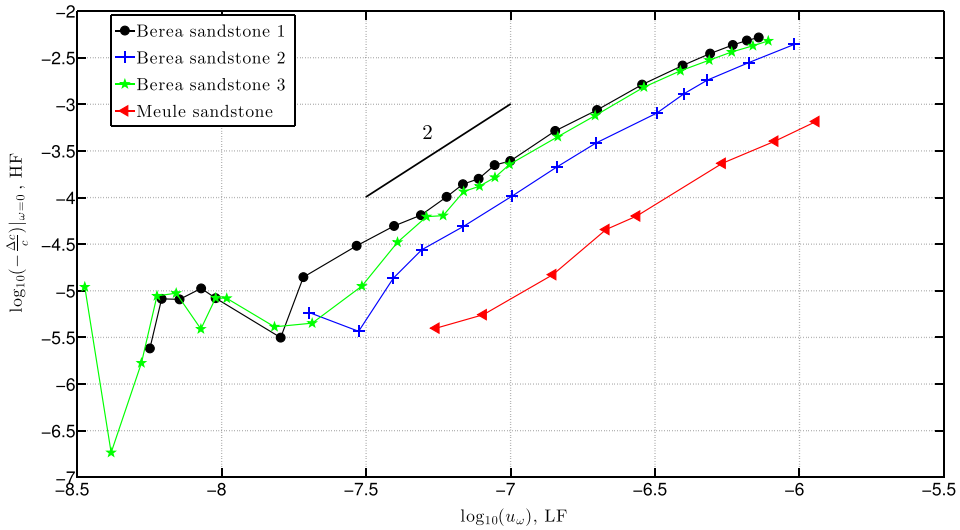

FIG. 8. Amplitude dependence of the offset ($\frac{\Delta c}{c}|_{\omega=0}$) for three samples of Berea and one sample of Meule sandstones. This offset is clearly visible in Figs. 2(b) and 4. A nearly quadratic dependence is found for the four rocks.

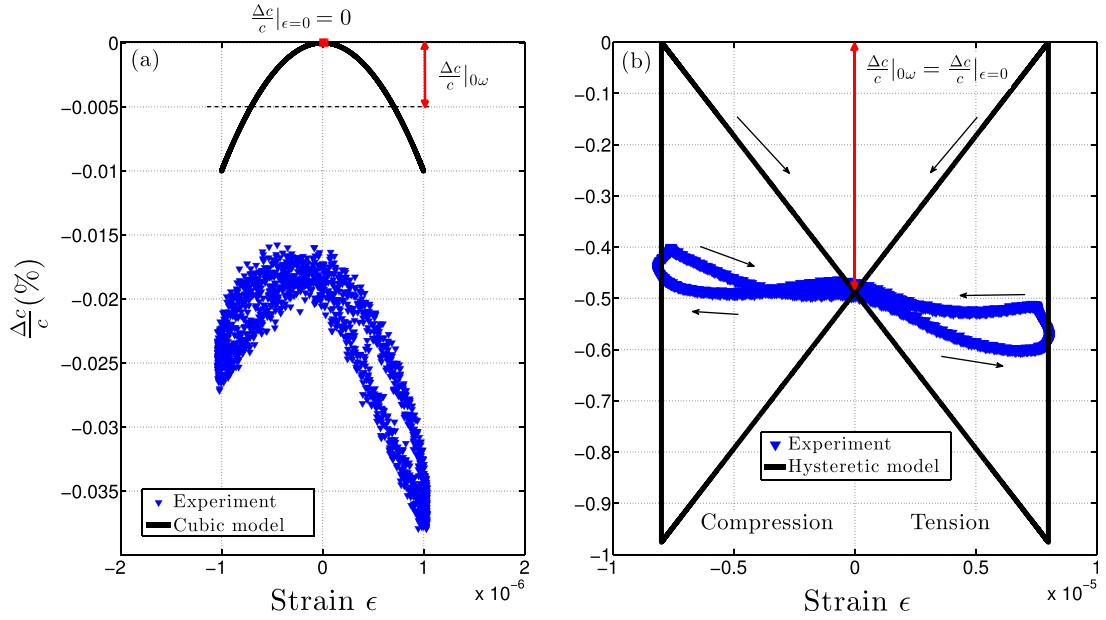

FIG. 9. Comparison model/experiment. (a) Comparison between experiment and the cubic elastic nonlinear model (cubic part of Eq. (7), i.e., $\beta = \alpha = 0$). The experimental curve presented here is the same as the one presented in Fig. 4 for an intermediate amplitude of excitation ($\epsilon = 10^{-6}$). Coefficient $\delta = -2 \times 10^8$ is chosen such that curvatures of the experimental data and the model are similar. The cubic elastic nonlinear model does not predict a non zero $\frac{\Delta c}{c}$-intercept as found in the experiment. (b) Comparison between experiment and the quadratic hysteretic elastic nonlinear model (hysteretic part of Eq. (7), i.e., $\beta = \delta = 0$). The experimental curve presented here is the same as the one presented in Fig. 4 for the highest amplitude of excitation. The quadratic hysteretic nonlinear model does predict an offset equal to the $\frac{\Delta c}{c}$-intercept, as approximately found in the experiment for highest strain amplitudes ($\frac{\Delta c}{c}|_{0\omega} \simeq \frac{\Delta c}{c}|_{\epsilon=0}$). Coefficient $\alpha = -1200$ is fitted such that both curves have the same offset, and with $\epsilon_m = 8.10^{-6}$, the maximum strain experienced by the material. In that case, the hysteresis is much larger in the model than in the experiment.

and the sample recovers slowly to its original state after the excitation is turned off. This is the well known phenomenon of slow dynamics.[7] The "soft-ratched" model,[24] based on bond restoration and rupturation, could *a priori* predict the offset and the $\frac{\Delta c}{c}$-intercept, as well as a modified version of the Preisach-Mayergoyz theory,[33] where hysteretic units can be either rigid or elastic.[23] These models have been originally developed for comparison with average based methods (e.g., Nonlinear Resonance Ultrasound Spectroscopy (NRUS)). Modifications of some of these models are currently in progress to simulate DAE experiments. As summarized in Table I, both models could potentially predict the complexity of conditioning/slow dynamics effects observed with DAE, as well as the amplitude dependence of the harmonic content. Modeling of these phenomena could also potentially help in understanding the scaling change observed at high strains (Fig. 6). Table I highlights the difficulty to describe the wealth of observations with a minimum of parameters. For application purposes, it might be relevant to concentrate only on the modeling of few phenomena to ultimately have the ability to perform the inverse problem. In particular, we think that efforts have to be carried out to describe conditioning/slow dynamics effects that are dominant over hysteretic behaviors.

3. Influence of the ultrasonic probe amplitude

DAE results are performed using a 10 V-amplitude ultrasonic probe source. This voltage allows one to obtain low-noise measurements for both nonlinear elastic (Fig. 4) and dissipative (not shown in Refs. 3–5) signatures. The 10 V-amplitude corresponds roughly to a strain $\epsilon^{US} = 10^{-6}$ (strain value is found using a laser vibrometer), while the LF strain ϵ^{LF} is in the range of $[3.10^{-8} \rightarrow 10^{-5}]$. Thus, the qualification of probe and pump waves can be misleading at low LF strain when $\epsilon^{LF} < \epsilon^{US}$.

To confirm our assumption that the ultrasonic signal just reads the elastic state of the sample modulated by the LF pump excitation, we perform DAE at two different ultrasonic probe amplitudes: either 10 V or 1 V is sent to the US emitter which corresponds, respectively, to $\epsilon^{US} = 10^{-6}$ and 10^{-7}. Voltage below 1 V results into noisy measurements. These DAE measurements are performed at two LF strain ($\epsilon^{LF} = 10^{-6}$ and 10^{-5}). Each measurement is performed three times. Each signature is the average of ten acquisitions, and we wait 30 s between each pump excitation. Because conditioning can also affect the measurement (30 s is not enough to completely recover, see Sec. II B), we alternate one measurement with 10 V, one with 1 V, etc.

For intermediate LF strain ($\epsilon^{LF} = 10^{-6}$) in Fig. 10(a), no difference is observed whether US pulses are launched with 10 or 1 V. Signatures are also visually similar at high LF strain ($\epsilon^{LF} = 10^{-5}$) in Fig. 10(b). However, we observe an increasing offset with experiment number (offset Exp. 1 < offset Exp. 3 < offset Exp. 5) due to conditioning. Further, the offset is slightly smaller with 1 V than with 10 V (offset Exp. 6 < offset Exp. 5; offset Exp. 4 < offset Exp. 3; offset Exp. 2 < offset Exp. 1). This suggests that the ultrasonic probe slightly increases the offset when launched at 10 V ($\epsilon^{US} = 10^{-6}$), participating modestly to the conditioning. The ultrasonic probe contribution to the global conditioning is, however, much smaller than the conditioning induced by the LF pump field.

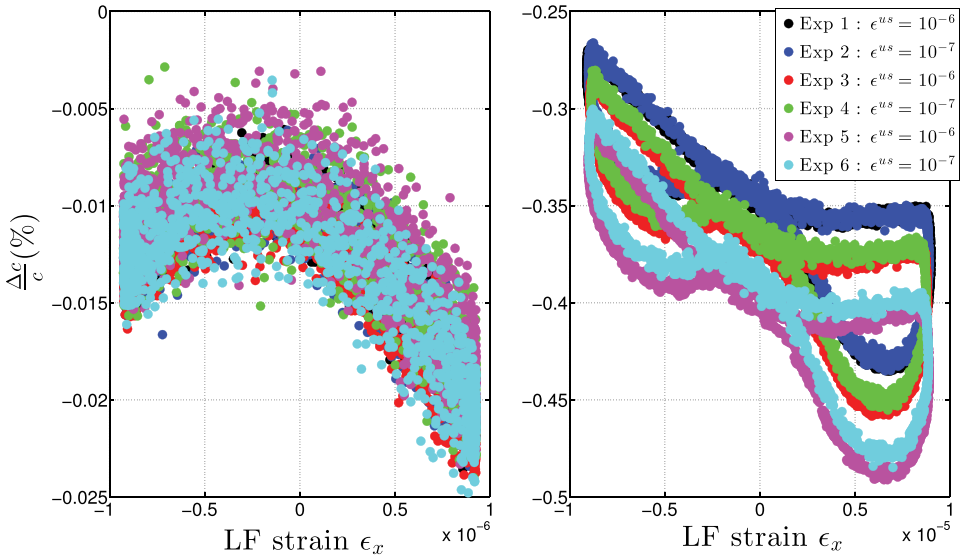

FIG. 10. Influence of the ultrasonic pulse amplitude on DAE signatures. (a) 10^{-6}-LF strain. No change is observed whether ultrasonic pulse amplitude is 10^{-7} or 10^{-6}. (b) 10^{-5}-LF strain. Signatures are also visually similar at high LF strain. However, we observe an increasing offset with experiment number (offset Exp. 1 < offset Exp. 3 < offset Exp. 5) due to conditioning. And the offset is slightly smaller with $\epsilon^{us} = 10^{-7}$ than with $\epsilon^{us} = 10^{-6}$ (offset Exp. 6 < offset Exp. 5; offset Exp. 4 < offset Exp. 3; offset Exp. 2 < offset Exp. 1). This suggests that the ultrasonic probe slightly affects the offset when launched at 10 V, participating modestly to the conditioning.

B. Resonant low frequency field

1. "Steady-state" regime of the harmonic content

The different scalings presented in Sec. III A (Figs. 5–8) were extracted in the steady-state regime, i.e., between 0.1 and 0.3 s in Fig. 2. Applying it on successive moving windows of 6 periods over the steady-state regime (Fig. 11(a)) allows one to observe the evolution of harmonic amplitudes in Fig. 11(d)–11(l). Such piecewise procedure could also be of great interest to analyze the HF field, but the down sampled HF signal is not long enough to properly extract its harmonic content (the excitation length is limited by the memory of the acquisition card). However, low pass filtering of the HF signal allows one to follow the evolution of the offset (Figs. 11(b) and 11(c)). One can clearly see from Fig. 11 that an actual steady-state (between 0.1 and 0.3 s) is not attained during our experiments, during the 0.3 s of excitation. Despite the constant amplitude of the fundamental displacement in Fig. 11(d), the offset slightly

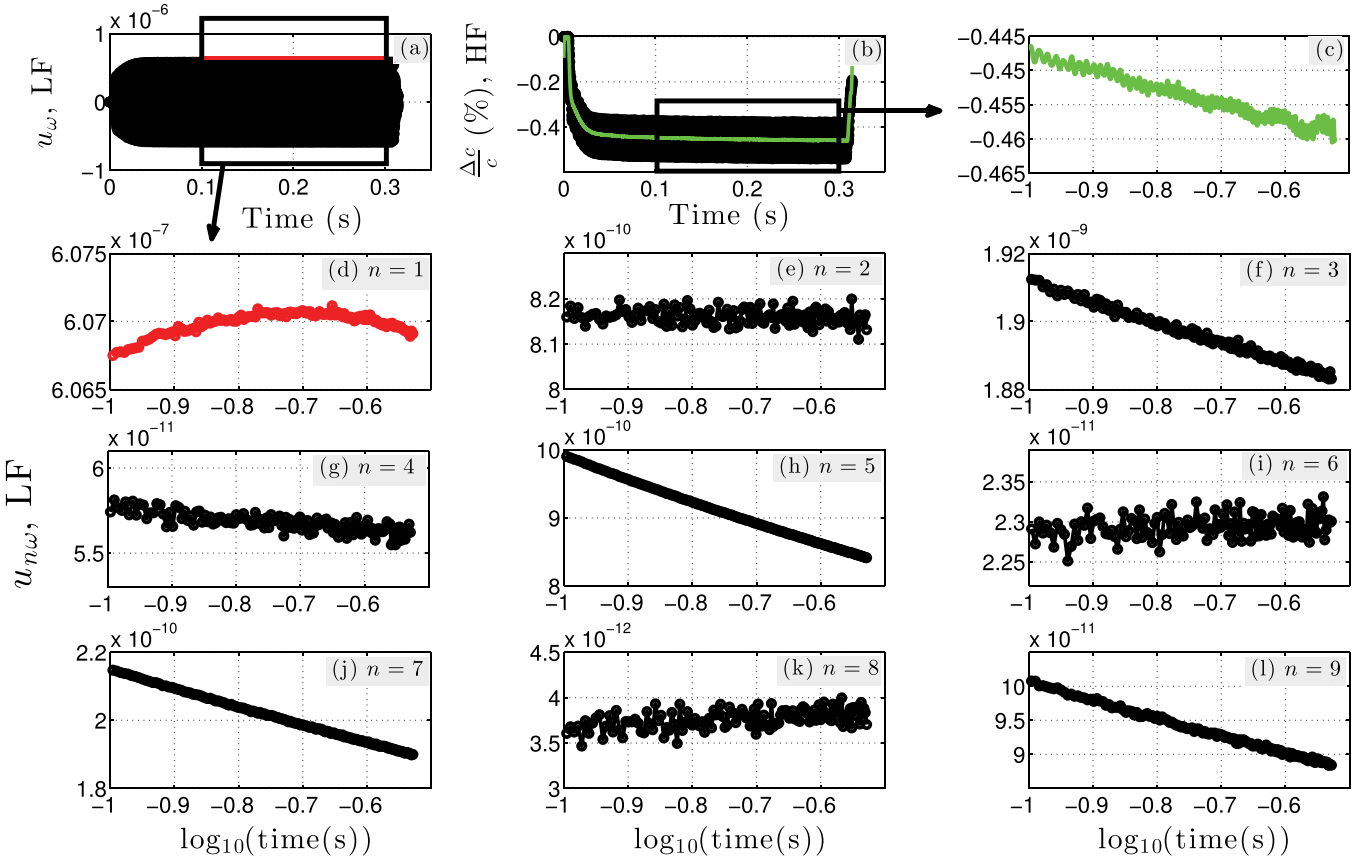

FIG. 11. Time dependence of the harmonic content. (a) Low frequency signal (displacement), similar to Fig. 2(a). (b) High frequency signal (relative velocity change), similar to Fig. 2(b). (c) Low pass filter of (b) to show the increase of the offset (in absolute value) in the "steady-state" regime (100 to 300 ms). (d)–(l) Time evolution of the harmonic content between 100 and 300 ms. A log(t)-decrease of odd harmonic amplitudes is observed and an actual steady state is not attained.

increases (in absolute value) in a log(t)-dependence and amplitudes of odd harmonics decrease with the same dependence. Amplitudes of even harmonics remain constant. This observation is related to the progressive conditioning of the material that takes place during the excitation. The increasing offset corresponds to a speed of sound decrease with excitation time, similarly to the decrease in the resonance frequency with conditioning (Fig. 3 of Ref. 7). Simultaneously to the progressive time delay, we observe an increase in attenuation for all our tested samples,[35] i.e., the amplitude of US pulses decreases with a similar time dependence (not shown). To our knowledge, the decrease in amplitude of odd harmonics with excitation time due to conditioning has not been reported elsewhere. This observation confirms that conditioning affects the nonlinear elasticity. The decrease in odd harmonic amplitudes may be related to a decrease in hysteretic elastic nonlinearity, affecting only odd harmonics (or a decrease in classical cubic elastic nonlinearity for the third harmonic). However, we observe that the offset in Fig. 11(c) keeps increasing, suggesting that the nonlinearity slightly increases with excitation time (i.e., conditioning). These observations seem contradictory *a priori*, but it suggests that new nonlinear models have to be developed to properly take into account the conditioning effects.[24,36,38] In Ref. 37, authors show that longer the conditioning, the higher is the global measured nonlinearity (fundamental + harmonics; Fig. 9 of Ref. 37). This result seems relevant with the increasing offset, but contradictory with the decrease in odd harmonics. Modeling work based on new physical insights[38] or modified version of existing model to simulate DAE measurements (PM-space based model[23,36]), are currently in development to clarify this point.

Fig. 11 presents the evolution of the harmonic content and the offset for only one amplitude of excitation in the Berea ($\epsilon_x = 6.10^{-6}$). The same analysis for all other amplitudes reveals some more complex behaviors, particularly for the third harmonic. Indeed, all odd harmonics decrease with excitation time at all strain amplitudes, with the exception of the amplitude of the third harmonic which displays a more complex behavior for several strain amplitudes. This might be related to the fact that the third harmonic amplitude has two contributions having the same order of magnitude: one due to the hysteretic behavior which affects all odd harmonics, and a second one due to the classical nonlinearity, still of importance for the third harmonic (cubic nonlinearity, term δ of Eq. (7)). This point will not be developed further in this paper but will be pursued in future work.

Finally, the fact that the steady-state is not completely reached in 0.3 s does not affect scalings found in Sec. III A. Fig. 12 confirms this statement showing that the nonlinear signature does not significantly change with excitation time, only a slight decrease of the offset and the $\frac{\Delta c}{c}$-intercept can be seen in Fig. 12(c).

2. Modal shape measurements

a. Axial x-direction. To confirm our assumption that the displacement field in the bar is the $\lambda/4$ mode, we undertake an investigation of the mode shapes. To do this, we employ a fiber-optic differential laser vibrometer[39] (Polytec OFV 552) to measure the longitudinal particle velocity $\dot{u}_x$ along the sample length of a Berea sandstone while emitting from the LF source (Fig. 1(b)). Results of this measurement are displayed in Fig. 13. One can clearly observe the expected profile for the deduced displacement and strain (Figs. 13(a) and 13(b), respectively). Further, the region probed by US pulses in DAE at 20 mm from the fixed boundary has a maximum strain amplitude equal to the strain deduced from the accelerometer. This validates the

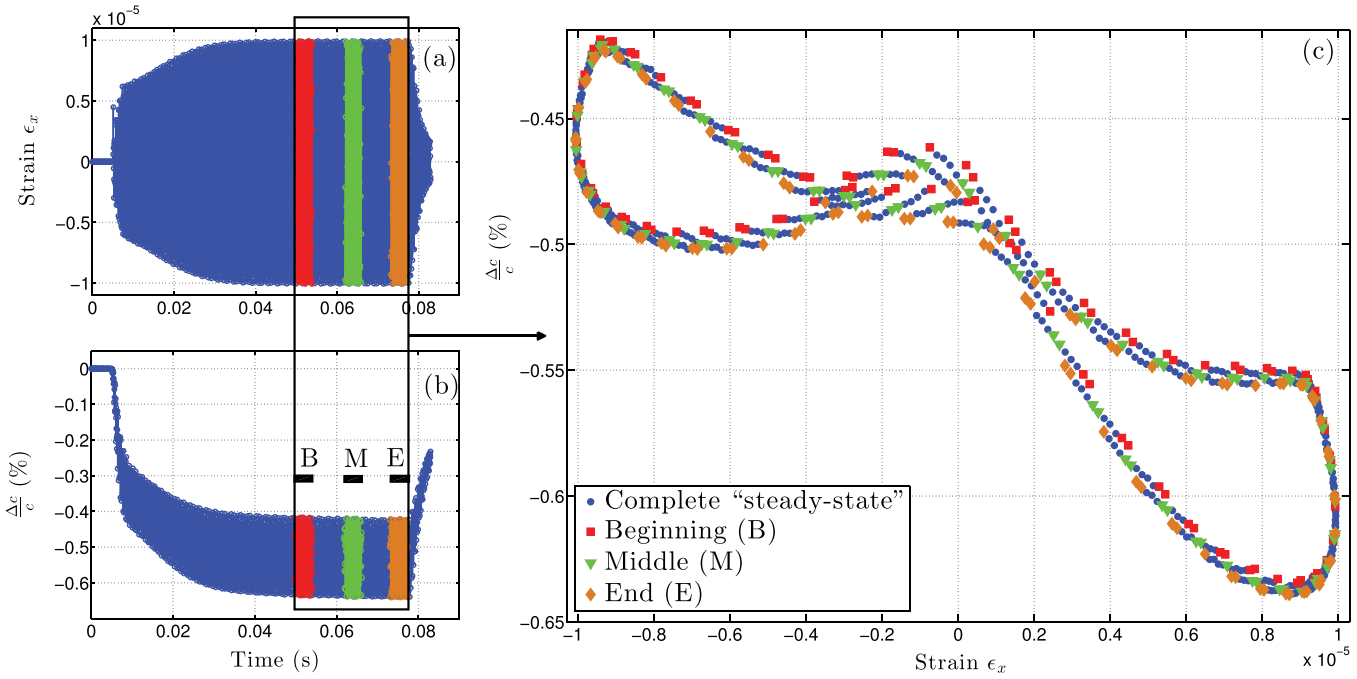

FIG. 12. Evolution of the nonlinear signature with time excitation in Berea sample for a 10^{-5} strain. (a) Low frequency strain *vs* time, similar to Fig. 2(a). (b) Relative velocity change *vs* time, similar to Fig. 2(b). (c) Relative velocity change *vs* strain. A slight decrease of the offset and the $\frac{\Delta c}{c}$-intercept is visible with time excitation due to sample conditioning. Note that conditioning only modestly affects amplitude dependences found in Fig. 6.

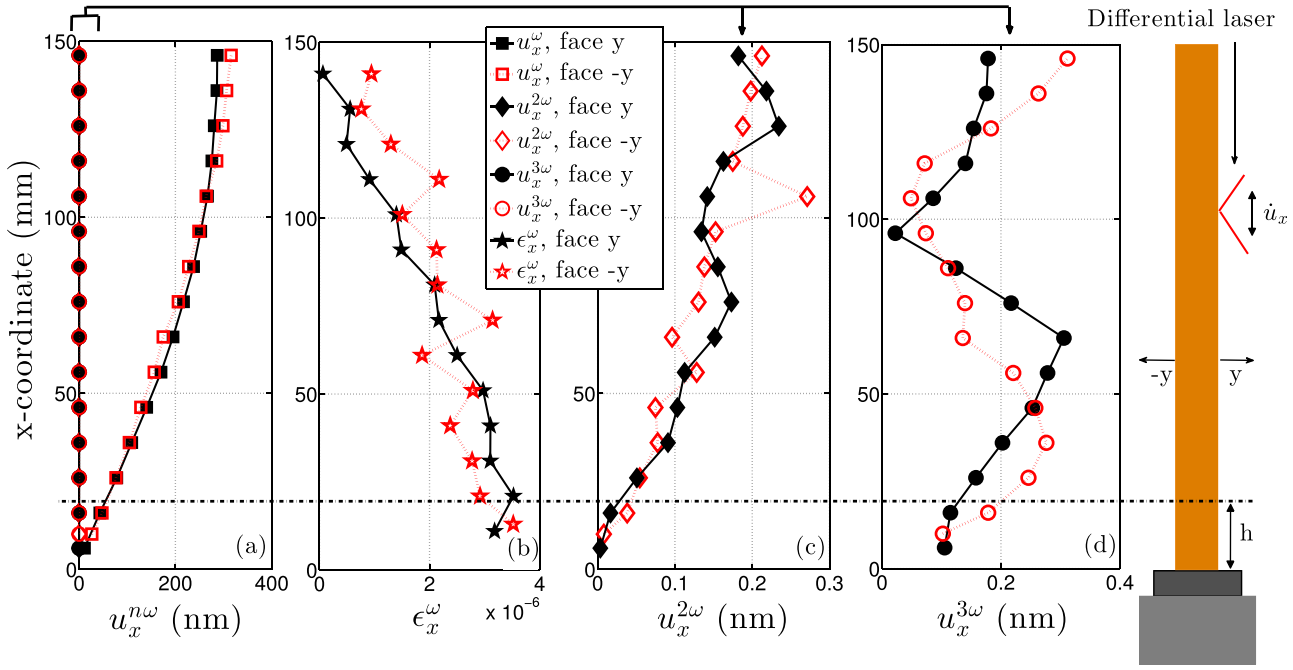

FIG. 13. The axial velocity $\dot{u}_x$ is measured along the sample length (Berea) on opposite sides of the sample (lines perpendicular to y and $-y$), at the frequency of the first compressional mode (≃4000 Hz). (a) Axial displacement deduced from the axial velocity at ω, 2ω, and 3ω. We observe the expected quarter wavelength profile obtained for the first compression mode. (b) Strain profile deduced from the axial displacement at the fundamental frequency, also predicted by theory. (c) Displacement profile at the second harmonic. The profile experimentally obtained qualitatively agrees with the theory (Fig. 15(b), appendix A 2). (d) Displacement profile at the third harmonic. The profile also qualitatively agrees with the theory (Fig. 16(a), appendix B).

assumption made to deduce the strain amplitude in the probed region from the acceleration measured at the free end of the sample $\epsilon_x(h,t) \simeq \epsilon_x(0,t) = -\ddot{u}_x(L,t)/(8\pi L f_{LF}^2)$. Displacement amplitudes at 2ω and 3ω are also tracked and can be compared to theory (appendix A 2 and B, respectively). Harmonic amplitudes are three orders of magnitude smaller than the fundamental as seen in Fig. 13(a), and their spatial structure qualitatively agrees with theoretical predictions (Figs. 13(c) and 13(d)). Therefore, the higher harmonic axial displacements have a negligible effect on DAE measurements (the HF field).

b. Radial y-direction. Another measurement is made to measure $\dot{u}_y$ instead of $\dot{u}_x$ along the sample length, to capture the modal shape of the first compressional mode through the Poisson effect (Fig. 1(b)). Profiles obtained on both sides of the sample in Fig. 14(a) are not the Poisson version of the

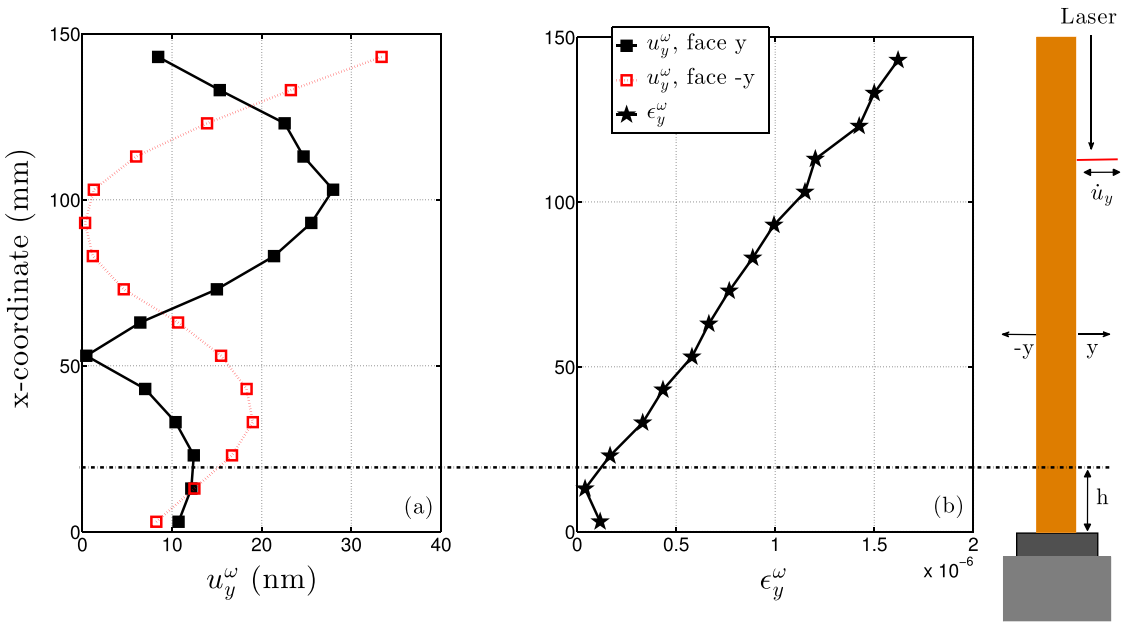

FIG. 14. The radial velocity $\dot{u}_y$ is measured along the sample length (Berea) on opposite sides of the sample (lines perpendicular to y and $-y$), at the frequency of the first compressional mode (≃4000 Hz). (a) Radial displacement deduced from the radial velocity on both sides of the samples. Displacement profiles obtained are not the Poisson version of the axial profile obtained in Fig. 13. (b) Temporal displacement signals obtained on both sides of the sample are added to obtain the differential displacement profile Δu_y^{ω}. Radial strain is then estimated using $\epsilon_y^{\omega} = \Delta u_y^{\omega}/d$.

axial profile obtained in Fig. 13(a), and appear to be influenced by adjacent bending/torsion modes. The closest non compressional modes are present at 5000 and 5500 Hz for the Berea sample. It is worth noting that the two displacement modal shapes measured on each side of the sample are not symmetric, which reveals the presence of a complex vibrational behavior, with possibly two different adjacent modes influencing the compressional mode. Both temporal displacement signals measured on each side of the sample are then added to obtain the differential radial displacement Δu_y^ω. This quantity tracks whether displacements on each side of the sample occur in phase or not, and whether radial strain is involved. This differential displacement is converted into radial strain using $\epsilon_y^\omega = \Delta u_y^\omega / d$ (Fig. 14(b)). Despite the complexity of displacement profiles originally measured, the deduced radial strain profile appears to be simple, with one single node located near the fixed boundary. However, this profile is not the Poisson version of the axial strain profile found in Fig. 13(b) (both profiles should look similar). There is no clear interpretation on why such a radial profile is found, with radial strain reaching its maximum at the free end of the bar. Since the largest displacements occur at the free end of the bar, irregular geometry could be one of the reasons for this result. Indeed, axial displacement is 300 nm (Fig. 13(a)) at the free end of the bar, while 30 nm-radial displacement is measured (Fig. 14(a)). This would give an angular irregularity of $arctan(30/300) \simeq 5.7°$. This value is probably too large to entirely explain this unexpected result, but it may be part of it. With the same idea in mind, if a torsion motion due to adjacent mode is present and if the rod sample is not perfectly circular, this could contribute to artificially high radial strain values. Nevertheless, it is of interest to observe that the radial strain seems to be very small in the probed region: $\epsilon_y^\omega(h,t) < 3 \times 10^{-7}$ as opposed to $\epsilon_x^\omega(h,t) = 3.5 \times 10^{-6}$ in the axial direction, i.e., more than 10 times smaller. Strain in the probed region is therefore primarily in the axial direction as required to perform reliable DAE measurements.

Finally, this detailed measurement shows that axial strain modal shapes experimentally measured are those expected theoretically for the first compressional mode of the sample. Spatial structures of harmonics measured at 2ω and 3ω are also qualitatively close to the theory. This experimental work supports the assumption of a non-disturbed compressional mode, despite the complexity found when measuring radially, possibly due to adjacent modes and/or slightly irregular geometry. In any case, one can try to minimize the influence of adjacent modes by choosing an appropriate length/diameter ratio for each sample, to prevent the frequency of the compressional mode to be too close to the frequency of bending/torsion modes. Further, maximizing the diameter and probing near the fixed boundary certainly help to reduce the influence of torsion/bending modes, but still keeping in mind that the US time of flight must be much smaller than the LF period to perform a reliable DAE measurement.

IV. CONCLUSION

This work aims at exploring experimental considerations in applying the dynamic acousto-elasticity method, as well as making quantitative comparisons to existing theories. We introduce a projection procedure in order to quantitatively extract harmonics. We compare LF and HF fields and show that both can be described by the nonlinear quadratic elastic model. Further, the higher harmonic content extracted is in agreement with previous results obtained in rocks with other methods [NRUS, for instance]. Several differences between experimental data and existing theories are, however, highlighted (Table I). The power-law amplitude dependence for harmonics greater than $2f$ progressively decreases for strains higher than 10^{-6}. This phenomenon is related to acoustic conditioning that brings the material to a metastable state at each new amplitude excitation. The amplitude dependent attenuation that comes from the nonlinear hysteretic behavior may also be a second reason for the scaling changes observed for the LF field. Current modeling work, which combines nonlinear hysteretic behaviors and conditioning/relaxation, will certainly help in understanding these observations.[23,24,36,38]

The second part of this work aims at clarifying several points related to the resonant LF field. We show experimentally that the expected quarter wavelength profile is present in our sample. Several suggestions are given to minimize the influence of adjacent resonant modes near the first compressional mode. We also show that the LF harmonic content has a negligible influence on DAE results. In addition, the careful study of the steady-state regime allows one to observe the effect of the conditioning on DAE results and the evolution of the harmonic content due to this conditioning. This observation emphasizes the fact that modeling of conditioning/slow dynamics is of utmost importance to accurately describe the elasticity of rocks, cracked materials, etc. It is also worth noting that the comparison made between both fields can be applied to any pump-probe measurement scheme and the analysis of the steady-state can be applied to any nonlinear resonant method.

DAE provides new information regarding the nonlinear elastic properties of materials compared to other acoustical methods (wave frequency mixing or resonance based measurements) because it provides the full dynamic cycle (including hysteresis and memory effects), as well as a more complete description of the acoustic conditioning (offset and $\frac{\Delta c}{c}$-intercept), revealing some important differences with existing theories. In comparison with quasi-static acousto-elasticity that only characterize the compressional phase, DAE has the advantage to probe both tensile and compressional states in a single experiment, and for smaller strains (closer from the equilibrium state). For application purposes, DAE has the advantage of probing the sample locally, making it relevant for imaging in various fields such as non destructive testing, medical imaging (bones, contrast agents, etc), and rock physics/seismology. In particular, one of the current research topics in seismology is to use tidal forces for the low frequency field, and passive noise or earthquake seismicity as the probe.

ACKNOWLEDGMENTS

We thank P.-Y. Le Bas, T. J. Ulrich, J. A. TenCate, C. Larmat, B. E. Anderson, K. Van Den Abeele and M. Scalerandi, T. Gallot, and S. Haupert for helpful discussions.

This work was supported by the US Department of Energy, Office of Basic Energy Sciences.

APPENDIX A: QUADRATIC ELASTIC NONLINEAR THEORY AND DAE

1. Wave equations

This appendix theoretically describes the dynamic acousto-elasticity measurement assuming a simple quadratic elastic nonlinearity, implying third order elastic constants A, B, C.[2] This description implies an isotropic material and is used in Sec. III A 1 to verify the consistency of both wave fields. Similarly to standard acousto-elastic experiments (i.e., static version of this experiment), the propagation of low amplitude ultrasonic pulses within the sample is modulated by a high amplitude change in the strain field. Regarding the particular setup (Fig. 1), where the longitudinal ultrasonic waves propagate perpendicularly to the uniaxial quasi-static field, the equation of motion for the high frequency pulses is given by (Chapter 3 of Ref. 6)

$$\rho \frac{\partial^2 u_y}{\partial t^2} = \frac{\partial}{\partial y}[K_0(1+\beta_y \epsilon_x)\epsilon_y] \tag{A1}$$

with

$$\beta_y = \frac{K - \frac{2}{3}\mu + 2B + 2C}{K_0}, \tag{A2}$$

where K_0, K, and μ are the longitudinal, bulk, and shear moduli, respectively. $\epsilon_x = \partial u_x/\partial x$ and $\epsilon_y = \partial u_y/\partial y$ denote the longitudinal strain in each direction. Similarly, the LF strain field obeys[6]

$$\rho \frac{\partial^2 u_x}{\partial t^2} = \frac{\partial}{\partial x}[K_0(1+\beta_x \epsilon_x)\epsilon_x] + F(t)\delta(0) \tag{A3}$$

with

$$\beta_x = \frac{\frac{3}{2}K + 2\mu + A + 3B + C}{K_0}. \tag{A4}$$

F is the LF source driving the sample, located at the fixed boundary ($0 < x < L$, where coordinates 0 and L are the fixed and free boundaries, respectively). From Eqs. (A1) and (A3), it follows that β_y involves the coupling $\epsilon_x\epsilon_y$, whereas β_x involves the coupling of ϵ_x with itself (term ϵ_x^2). Therefore, for a purely quadratic nonlinearity, the quantity $\frac{\Delta c}{c}|_{2\omega}$ obtained by projecting onto ω-functions should be proportional to u_ω, with a slope proportional to β_y. Further, $u_{2\omega}$ should be proportional to u_ω^2, with a slope proportional to β_x. From Table 11.1 of Ref. 6, one finds $\beta_x \simeq 2\beta_y$.

2. "Modal" shape of the 2ω-signal

Having these scales in mind, we now quickly pay attention to the forced regime of the LF field. Indeed, the frequency of the source F is tuned to a quarter wavelength resonance, creating a standing wave within the sample. The second harmonic generated within the sample does not meet simple boundary conditions to resonate and its presence along the bar is more complex. To solve this problem,[6,33] one can use a hierarchy of equations to solve Eq. (A3), replacing u_x by $u_\omega(t) = \xi u_\omega^{(1)}(t) + \xi^2 u_\omega^{(2)}(t)$ and F by ξF, where ξ helps grouping terms of the same order of magnitude. The subscript ω denotes that the Fourier representation of Eq. (A3) is used to solve it.[6,33] At the free end of the bar, one finds

$$u_\omega^{(1)}(L) = -\frac{C_1}{2}[G_{\omega 0}(L|0)\delta(\omega-\omega_0) + G_{-\omega 0}(L|0)\delta(\omega+\omega_0))], \tag{A5}$$

where $G_{\omega 0}(L|0)$ is the Green function for propagation from 0 to L (fix to free end). This first term gives the linear solution of the equation and is used to calculate $u_\omega^{(2)}(L)$

$$u_\omega^{(2)}(L) = C_2 \int_0^L dx \frac{\partial}{\partial x} G_{2\omega_0}(L|x) \frac{\partial}{\partial x} G_{\omega_0}(x|0) \times \frac{\partial}{\partial x} G_{\omega_0}(x|0)\delta(\omega - 2\omega_0), \tag{A6}$$

where $C_2 \propto \beta_x C_1^2$. $u_\omega^{(2)}(L)$ only exists for $\omega = 2\omega_0$ and then represents the displacement of the second harmonic within the sample. This equation emphasizes the idea that the source of the second harmonic is distributed along the bar (term $G_{\omega_0}(x|0)$), and that each source at 2ω is carried throughout the sample by the 2ω-term $G_{2\omega_0}(L|x)$.

Numerical implementation of Eq. (A6) gives several indications for our problematic. First, the maximum strain amplitude at 2ω in Fig. 15(c) is found near the sample center ($x \simeq 0.65L$ here, depending on attenuation), whereas it reaches zero on both edges of the bar. This particular shape is a compromise between the fact that (i) the ω-source is higher near the fixed boundary (Fig. 15(a)), (ii) the 2ω-signal grows with propagation distance, and (iii) boundary conditions impose a null strain at the free end of the bar. The displacement profile in Fig. 15(b) can be compared with experimental curve found in Fig. 13(c).

The second lesson of this theoretical part is that the 2ω-signal at the free end is found 90° out of phase with the fundamental. These findings are compared with experimental results in Sec. III.

APPENDIX B: HYSTERETIC ELASTIC NONLINEARITY: "MODAL" SHAPES OF ODD HARMONICS

This appendix aims at describing the spatial structure of odd harmonics generated in the sample with fixed-free boundary conditions (Fig. 1), assuming simple hysteretic nonlinearity.

As background, we need the constitutive 1D-relation for material that has simple Preisach-Mayergoyz space nonlinearity,[6,16] assuming a uniform distribution of elementary hysteretic elements. The relevant formula is a pointwise formula for the stress-strain in a resonant bar[6]

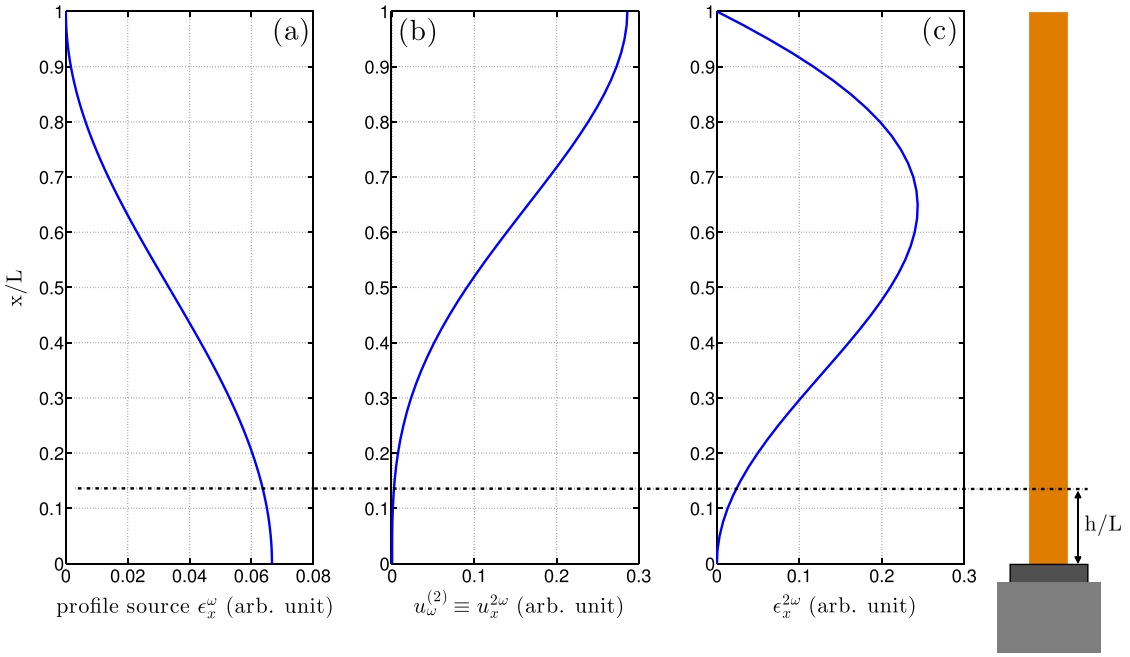

FIG. 15. Second harmonic generation along the bar assuming a quadratic elastic model. (a) Spatial profile of the source (axial strain) at the fundamental frequency ω. (b) Displacement profile of the second harmonic along the bar (Eq. (A6) gives the value in $x = L$). This spatial shape can be compared with experimental curve found in Fig. 13(c). A qualitative good agreement is found. (c) Strain profile deduced from the displacement profile. Maximum strain is found near the bar center.

$$\sigma = M\left[(1-\alpha\epsilon_m(x))\epsilon + \frac{\alpha}{2} sign(\dot{\epsilon})(\epsilon_m^2(x) - \epsilon^2)\right], \tag{B1}$$

where $\epsilon_m(x)$ is the magnitude of the strain excursion at x. The first term $(1-\alpha\epsilon_m(x))\epsilon$ on the RHS relates to the change in the behavior of the fundamental frequency. The second term is the source of the higher harmonics. We are interested in the latter, so write $u_x = u_0 + w$ and have

$$\begin{aligned}\frac{\partial^2 w}{\partial t^2} &= c^2\frac{\partial^2 w}{\partial x^2} + c^2\frac{\partial}{\partial x}\left[\frac{\alpha}{2} sign(\dot{\epsilon}_0)(\epsilon_{0m}^2(x) - \epsilon_0^2)\right] \\ &= c^2\frac{\partial^2 w}{\partial x^2} + c^2\frac{\partial}{\partial x}H(x,t),\end{aligned} \tag{B2}$$

where

$$\begin{aligned} u_0 &= U\sin k_1 x \sin\omega t, \\ \epsilon_0 &= k_1 U\cos k_1 x \sin\omega t, \\ k_1 &= \frac{\pi}{2L}, \quad \omega = k_1 c, \end{aligned} \tag{B3}$$

and

$$\epsilon_{0m} = k_1 U\cos k_1 x. \tag{B4}$$

On using the equation for ϵ_0 in Eq. (B2), the "source" term on the right becomes

$$H(x,t) \equiv \frac{\alpha}{2} sign(\dot{\epsilon}_0)(\epsilon_{0m}^2(x) - \epsilon_0^2) = h(x)m(t) \tag{B5}$$

with

$$\begin{aligned} h(x) &= \frac{\alpha}{2}(k_1 U\cos k_1 x)^2, \\ m(t) &= sign(\cos\omega t)\cos^2\omega t. \end{aligned} \tag{B6}$$

The spatial structure of the "source" caused by hysteresis is given by $h(x) \propto \cos^2 k_1 x$ (same source as the quadratic model in appendix A, see Fig. 15(a)), and the time dependence of this source is $m(t)$. It is shown that $m(t)$ can be represented as a power series in odd harmonics of the fundamental[33]

$$m(t) = \sum_{n=3,5,7,\cdots} \gamma_n \cos n\omega t, \tag{B7}$$

where

$$\gamma_n = \frac{8}{\pi}\frac{-1}{n(n^2-4)}\sin\frac{n\pi}{2}. \tag{B8}$$

Because the source in Eq. (B2) contains odd harmonics, we expand w as a power series in odd harmonics

$$w(x,t) = \sum_{n=3,5,7,\cdots} w_n(x)\cos n\omega t. \tag{B9}$$

Then,

$$\frac{\partial^2 w_n}{\partial x^2} = -(k_n)^2 w_n - \gamma_n \frac{\partial h(x)}{\partial x}. \tag{B10}$$

The solution to this equation, for the shape of the $\cos n\omega t$ mode, is

$$w_n = \int_0^L dx\ G_n(x|x')\ \frac{\partial h(x')}{\partial x'}, \tag{B11}$$

where G_n is the Green function associated with Eq. (B10). Before doing numerical work, one integration by parts is used

$$w_n = -\int_0^L dx \quad \frac{\partial G_n(x|x')}{\partial x'} \; h(x'). \tag{B12}$$

The Green functions are

$$\begin{aligned} G_n(x > x') &= \frac{1}{k_n \cos k_n L} \; \cos k_n(L - x) \; \sin k_n x', \\ G_n(x < x') &= \frac{1}{k_n \cos k_n L} \; \sin k_n x \; \cos k_n(L - x') \end{aligned} \tag{B13}$$

with $k_n = n\pi/(2L)$.

The source function goes as $\cos^2 k_1 x$ and is distributed throughout the bar although concentrated near $x = 0$ (Fig. 15(a)). The spatial structure of odd harmonics $n = 3, 5, 7, 9$ are shown in Fig. 16. These modes have a shape more or less like the free modes of the bar, $\sin k_n x$, but are distorted from this shape by the distributed source.

From this description, several conclusions can be highlighted:

(1) The strain behavior of hysteretic elastic elements leads to an interior source that is spatially distributed and moves in time with the odd harmonics of the fundamental. It is the fundamental that is driven by the external source.
(2) The spatial structure of the odd harmonics is qualitatively similar to the spatial structure of the free vibrations. A probe located along the axis of the bar will see each odd harmonic through the β nonlinear coupling. The amplitudes of the odd harmonics scale at $(k_1 U)^2$ (Eq. (B5)). The relative amplitude of each odd harmonic depends on the amplitudes in Eq. (B8) and on where the probe encounters the harmonic.
(3) The time dependence of the odd harmonics is $\cos n\omega t$, out of phase with the fundamental at $\sin \omega t$. This result can be compared with experimental findings in Fig. 7.

APPENDIX C: GRAM-SCHMIDT PROCESS

The Gram-Schmidt process allows one to build a set of orthonormal functions. The set of functions that we need to analyze our data are a series of sine and cosine functions with frequencies ranging from the fundamental (pulsation ω) up to the nth harmonic ($n\omega$) to extract the harmonic content. The main interest in using this method is that we can extract the frequency content of a signal that is poorly sampled. For example, the signal in Figs. 2(b) and 2(d) contains information at the fundamental ($f \simeq 4000$ Hz) and harmonic frequencies ($2f$, $3f$,…), but its sampling rate is only 10 kHz (corresponding to the repetition rate of the HF pulse).

The following recipe is applied to build the set of orthonormal functions. All the functions are introduced one by one, making sure that each is orthogonal with previously introduced functions. The first function is a sine at the fundamental

$$S_1(t_k) = \frac{\sin(\omega t_k)}{\sqrt{\sum_{k=1}^{M} \sin^2(\omega t_k)}}, \tag{C1}$$

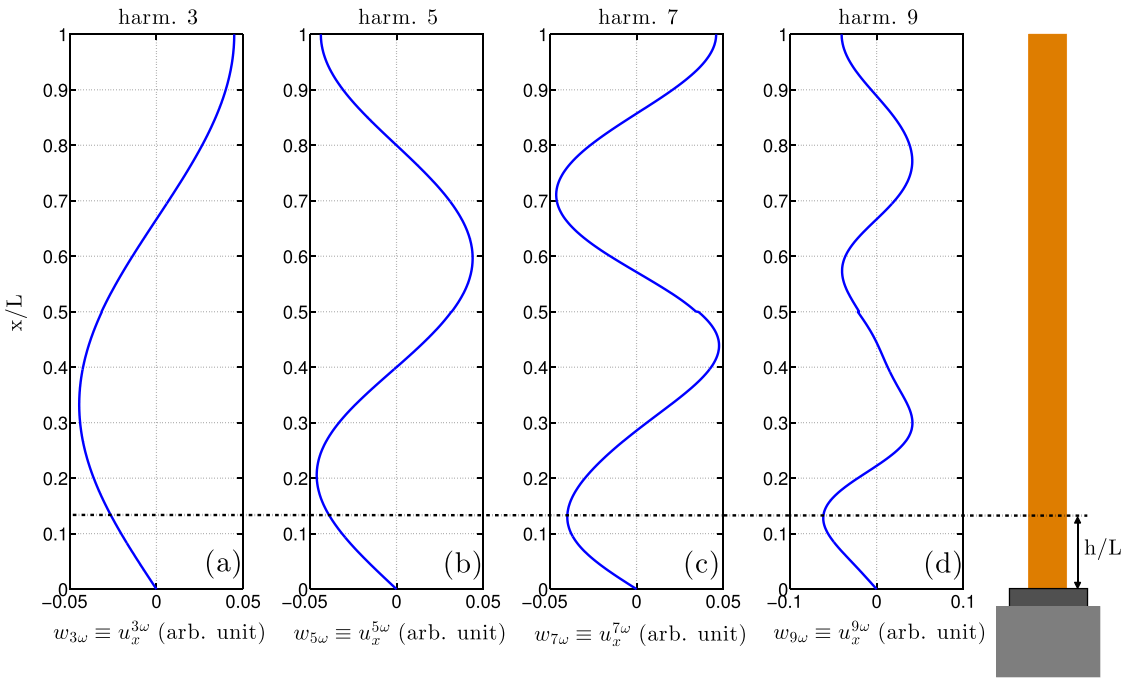

FIG. 16. Axial displacement profile of odd harmonics along the bar assuming a simple hysteretic elastic model (Eq. (B12)). Because these harmonics meet appropriate fixed-free boundary conditions to resonate, spatial shapes are similar to theoretical compressional modes: only the distributed source along the bar slightly modifies them. (a) Third harmonic. This spatial shape can be compared with experimental curve found in Fig. 13(d). A qualitative good agreement is found. (b) Fifth harmonic. (c) Seventh harmonic. (d) Ninth harmonic.

where the denominator allows one to norm the function. M is the total number of points of the original signal. The second function is a cosine at the fundamental frequency

$$C_1(t_k) = \frac{\cos(\omega t_k) - \left[\sum_{k=1}^{M} S_1(t_k)\cos(\omega t_k)\right] S_1(t_k)}{\sqrt{\sum_{k=1}^{M} \cos^2(\omega t_k)}}. \quad \text{(C2)}$$

The second term of the numerator orthogonalizes C_1 with the previous function S_1. This orthogonalization is needed because of finite length signals and rounding errors during the numerical implementation. A third function, sine at 2ω, is then introduced, orthogonalized with the two previous ones

$$S_2(t_k) = \frac{\sin(2\omega t_k) - \left[\sum_{k=1}^{M} S_1(t_k)\sin(2\omega t_k)\right] S_1(t_k) - \left[\sum_{k=1}^{M} C_1(t_k)\sin(2\omega t_k)\right] C_1(t_k)}{\sqrt{\sum_{k=1}^{M} \sin^2(2\omega t_k)}}. \quad \text{(C3)}$$

This recipe can be applied until S_n and C_n, n being determined according to the harmonic content. One can also imagine choosing some functions at $n\omega/2$ in the case of subharmonic frequencies. When the signal is poorly sampled, one needs a fairly long signal to be able to extract the highest harmonic content. That is the reason why the error increases in Fig. 3(b), when N is chosen too high. Variables q_n and r_n are used in Eq. (3) for notation simplicity.

Orthonormality can be checked making sure that

$$\begin{aligned} \langle S_m | S_p \rangle &\equiv \sum_{k=1}^{M} S_m(t_k) S_p(t_k) = \delta_{m,p} \\ \langle C_m | C_p \rangle &\equiv \sum_{k=1}^{M} C_m(t_k) C_p(t_k) = \delta_{m,p} \\ \langle S_m | C_p \rangle &\equiv \sum_{k=1}^{M} S_n(t_k) C_n(t_k) = 0, \end{aligned} \quad \text{(C4)}$$

where $\delta_{m,p}$ is the Kronecker symbol ($\delta_{m,p} = 1$ if $m = p$, 0 otherwise).

[1]K. W. Winkler and L. McGowan, "Nonlinear acoustoelastic constants of dry and saturated rocks," J. Geophys. Res. **109**, B10204, doi: 10.1029/2004JB003262 (2004).
[2]L. D. Landau and E. M. Lifshitz, *Theory of Elasticity*, 3rd ed., Theoretical Physics, Vol. 7 (Butterworth-Heinemann, 1986).
[3]G. Renaud, J. Rivière, S. Haupert, and P. Laugier, "Anisotropy of dynamic acoustoelasticity in limestone, influence of conditioning, and comparison with nonlinear resonance spectroscopy," J. Acoust. Soc. Am. **133**, 3706–3718 (2013).
[4]G. Renaud, P. Y. Le Bas, and P. A. Johnson, "Revealing highly complex elastic nonlinear (anelastic) behavior of earth materials applying a new probe: Dynamic acoustoelastic testing," J. Geophys. Res. **117**(B6), B06202, doi:10.1029/2011JB009127 (2012).
[5]G. Renaud, J. Rivière, P. Y. Le Bas, and P. A. Johnson, "Hysteretic nonlinear elasticity of berea sandstone at low vibrational strain revealed by dynamic acousto-elastic testing," Geophys. Res. Lett. **40**, 715–719, doi: 10.1002/grl.50150 (2013).
[6]R. A. Guyer and P. A. Johnson, *Nonlinear Mesoscopic Elasticity: The Complex Behaviour of Rocks, soil, concrete* (Wiley VCH, 2009).
[7]J. A. TenCate, "Slow dynamics of earth materials: An experimental overview," Pure Appl. Geophys. **168**(12), 2211–2219 (2011).
[8]U. Ingard and D. C. Pridmore-Brown, "Scattering of sound by sound," J. Acoust. Soc. Am. **28**(3), 367–369 (1956).
[9]P. J. Westervelt, "Scattering of sound by sound," J. Acoust. Soc. Am. **29**(8), 934–935 (1957).
[10]F. R. Rollins, Jr., L. H. Taylor, and P. H. Todd, Jr., "Ultrasonic study of three-phonon interactions. II. Experimental results,". Phys. Rev. **136**(3A), A597 (1964).
[11]L. H. Taylor and F. R. Rollins, Jr., "Ultrasonic study of three-phonon interactions. I. Theory," Phys. Rev. **136**(3A), A591 (1964).
[12]G. Renaud, S. Callé, and M. Defontaine, "Remote dynamic acoustoelastic testing: Elastic and dissipative acoustic nonlinearities measured under hydrostatic tension and compression," Appl. Phys. Lett. **94**, 011905 (2009).
[13]G. Renaud, S. Callé, and M. Defontaine, "Dynamic acoustoelastic testing of weakly pre-loaded unconsolidated water-saturated glass beads," J. Acoust. Soc. Am. **128**, 3344 (2010).
[14]I. Cespedes, Y. Huang, J. Ophir, and S. Spratt, "Methods for estimation of subsample time delays of digitized echo signals," Ultrason. Imaging **17**(2), 142–171 (1995).
[15]G. Renaud, M. Talmant, S. Callé, M. Defontaine, and P. Laugier, "Nonlinear elastodynamics in micro-inhomogeneous solids observed by head-wave based dynamic acoustoelastic testing," J. Acoust. Soc. Am. **130**(6), 3583–3589 (2011).
[16]K. E. A. Van Den Abeele, P. A. Johnson, R. A. Guyer, and K. R. McCall, "On the quasi-analytic treatment of hysteretic nonlinear response in elastic wave propagation," J. Acoust. Soc. Am. **101**, 1885–1898 (1997).
[17]V. Aleshin and K. Van Den Abeele, "Microcontact-based theory for acoustics in microdamaged materials," J. Mech. Phys. Solids **55**, 366–390 (2007).
[18]D. Pasqualini, K. Heitmann, J. A. TenCate, S. Habib, D. Higdon, and P. A. Johnson, "Nonequilibrium and nonlinear dynamics in berea and fontainebleau sandstones: Low-strain regime," J. Geophys. Res. **112**, B01204, doi: 10.1029/2006JB004264 (2007).
[19]K. Van Den Abeele and S. Vanaverbeke, "Multiscale approach and simulations of wave propagation and resonance in media with localized microdamage: 1-d and 2-d cases," in *Universality of Nonclassical Nonlinearity* (Springer, 2006), pp. 177–201.
[20]M. F. Hamilton and D. T. Blackstock, *Nonlinear acoustics* (Academic Press, 1998).
[21]K. E. A. Van Den Abeele, "Elastic pulsed wave propagation in media with second-or higher-order nonlinearity. Part I. Theoretical framework," J. Acoust. Soc. Am. **99**, 3334 (1996).
[22]R. A. Guyer, K. R. McCall, G. N. Boitnott, L. B. Hilbert, and T. J. Plona, "Quantitative implementation of preisach-mayergoyz space to find static and dynamic elastic moduli in rock," J. Geophys. Res. **102**, 5281–5293, doi:10.1029/96JB03740 (1997).
[23]P. P. Delsanto and M. Scalerandi, "Modeling nonclassical nonlinearity, conditioning, and slow dynamics effects in mesoscopic elastic materials," Phys. Rev. B **68**, 64107 (2003).
[24]O. O. Vakhnenko, V. O. Vakhnenko, and T. J. Shankland, "Soft-ratchet modeling of end-point memory in the nonlinear resonant response of sedimentary rocks," Phys. Rev. B **71**, 174103 (2005).
[25]V. Gusev and V. Tournat, "Amplitude- and frequency-dependent nonlinearities in the presence of thermally induced transitions in the preisach model of acoustic hysteresis," Phys. Rev. B **72**, 054104 (2005).
[26]K. V. D. Abeele and M. A. Breazeale, "Theoretical model to describe dispersive nonlinear properties of lead zirconate–titanate ceramics," J. Acoust. Soc. Am. **99**, 1430 (1996).

[27]V. Gusev, W. Lauriks, and J. Thoen, "Dispersion of nonlinearity, nonlinear dispersion, and absorption of sound in micro-inhomogeneous materials," J. Acoust. Soc. Am. **103**, 3216–3226 (1998).
[28]B. Capogrosso-Sansone and R. A. Guyer, "Dynamic model of hysteretic elastic systems," Phys. Rev. B **66**, 224101 (2002).
[29]V. Aleshin and K. V. D. Abeele, "Preisach analysis of the Hertz-Mindlin system," J. Mech. Phys. Solids **57**, 657–672 (2009).
[30]W. T. Yost and J. H. Cantrell, Jr., "Acoustic-radiation stress in solids. II. Experiment," Phys. Rev. B **30**(6), 3221 (1984).
[31]X. Jacob, R. Takatsu, C. Barriere, and D. Royer, "Experimental study of the acoustic radiation strain in solids," Appl. Phys. Lett. **88**, 134111 (2006).
[32]J. A. TenCate and T. J. Shankland, "Slow dynamics in the nonlinear elastic response of berea sandstone," Geophys. Res. Lett. **23**, 3019–3022, doi:10.1029/96GL02884 (1996).
[33]K. R. McCall and R. A. Guyer, "Equation of state and wave-propagation in hysteretic nonlinear elastic-materials," J. Geophys. Res. **99**, 23887–23897, doi:10.1029/94JB01941 (1994).
[34]T. A. Read, "The internal friction of single metal crystals," Phys. Rev. **58**, 371–380 (1940).
[35]V. Zaitsev, V. Gusev, and B. Castagnede, "Thermoelastic mechanism for logarithmic slow dynamics and memory in elastic wave interactions with individual cracks," Phys. Rev. Lett. **90**, 075501 (2003).
[36]M. Scalerandi, A. S. Gliozzi, C. L. E. Bruno, and P. Antonaci, "Nonequilibrium and hysteresis in solids: Disentangling conditioning from nonlinear elasticity," Phys. Rev. B **81**(10), 104114 (2010).
[37]M. Scalerandi, A. S. Gliozzi, C. L. E. Bruno, and P. Antonaci, "Nonequilibrium phenomena in damaged media and their effects on the elastic properties," J. Acoust. Soc. Am. **131**, 4304 (2012).
[38]L. Ostrovsky and A. Lebedev, "Modeling of processes in structurally nonlinear media with relaxation," AIP Conf. Proc. **1474**, 199 (2012).
[39]T. J. Ulrich, K. V. D. Abeele, P. Y. Le Bas, M. Griffa, B. E. Anderson, and R. A. Guyer, "Three component time reversal: Focusing vector components using a scalar source," J. Appl. Phys. **106**(11), 113504 (2009).